SOFT ROBOTICS
Volume 8, Number 3, 2021

DOI: 10.1089/soro.2020.0018

SoRo
Soft Robotics

ORIGINAL ARTICLE

Soft Actuators Based on Liquid–Vapor Phase Change Composites

Xiying Li,[1] Huiling Duan,[1,2] Pengyu Lv,[1] and Xin Yi[1]

Abstract

Liquid–vapor phase change materials (PCMs), capable of significant volume change, are emerging as attractive actuating components in forming advanced soft composites for robotic applications. However, the novel and functional design of these PCM composites is significantly limited due to the lacking of the fundamental understanding of the mechanical properties, which further inhibits the broad applications of PCM based materials in the engineering structures requiring large deformation and high loading capacity. In this study we fabricate PCM-elastomer composites exhibiting large deformation and high output stress. Thermomechanical properties of these composites are experimentally and theoretically investigated, demonstrating enhanced deformation and loading capacity due to the induced vapor pressure. By controlling the distribution and content of the PCM inclusions, structures with tunable deformability under a relatively small strain in comparison with traditional soft materials are fabricated. Accompanying with the asymmetrical friction and deformation, complex locomotion and adaptable grabbing function are achieved with excellent performance.

Keywords: phase change materials (PCMs), PCMs-elastomer composites, soft actuators, multimodal locomotion, liquid–vapor phase transition

Introduction

Smart soft materials owning elegant properties of simple operation, programmability, fast response, and tunable stiffness have wide applications in soft actuators, robots, artificial muscles, and so on.[1–5] Specific properties of these smart materials and ingenious design strategies endow the soft actuators with various functions and excellent performance.[6–12] For example, tendons made of shape memory alloys/polymers have become an important part in adapting robots due to the good shape programmability.[7] Cylindrical microrobots fabricated by photoactive liquid–crystal elastomers have the biomimetic motion under the actuation of structured monochromatic light.[10]

Compared with other smart soft materials, thermospneumatic actuation using liquid–vapor phase change in phase change materials (PCMs) has the advantages of simple fabrication, easy operation, lightweight, durability, large deformation, and high loading force[13–22] and has been utilized in various fields, such as valves in microfluidics,[13] triggers for standing scales,[14] and soft robots with locomotion and grabbing functions.[15,20] The volume change of capsuled liquid from liquid to vapor in chambers has been studied through the saturated vapor pressure,[14,16] revealing the capacity of large deformation. Nonetheless, the simple chamber design faces a huge risk of chamber damage, which limits the further applications.[16]

Phase change composites, embedding the PCMs into silicone rubber, combining the elastic properties of the rubber matrix, and extreme volume change accompanying liquid–vapor transition, decrease the risk of structural failure by reducing the chambers into uniformly distributed inclusions and have been applied in soft actuators.[17,18] Although the liquid–vapor phase transition in chambers has been discussed, the thermomechanical properties of these PCM-elastomer composites are rarely studied. Insufficient fundamental understanding of the thermomechanical properties of PCM-elastomer composites leads to limited usage of these soft composites merely as a complementary part to the design of soft actuators and advanced engineering structures.[17,18]

In this work, the thermomechanical properties of PCM-elastomer composites with liquid inclusions undergoing

[1]State Key Laboratory for Turbulence and Complex Systems, Department of Mechanics and Engineering Science, BIC-ESAT, College of Engineering, Peking University, Beijing, China.
[2]CAPT, HEDPS and IFSA Collaborative Innovation Center of MoE, Peking University, Beijing, China.

liquid–vapor phase transition are first investigated through the micromechanical method and verified by experimental studies. It is shown that the vapor pressure induced by the liquid–vapor transition in the inclusions could lead to enhanced thermal expansion and output stress without significant change of the material rigidity. By controlling the distribution and amount of PCM inclusions, increased deformability with wide tunability is achieved in curved beam structure. Actuating the folding of stiff sheets at the joints due to the high output stress, the PCM-elastomer composites serve as the actuators in designed deformable structures. Comparing previous structure designs with the performance reported here highlights the wide tunability in deformability at a relatively small strain. Through the assembly of deformable units, functional structures are fabricated with adjustable performance, such as adaptable grippers. Moreover, asymmetrical friction boundaries are introduced to achieve the locomotion of these deformable structures, such as unidirectional motion with carrying ability. Asymmetrical deformation of assembly structures is also realized to complete more complex motion such as turning.

Results and Discussion

Thermomechanical properties of PCM-elastomer composites

The PCM-elastomer composite is fabricated at room temperature and consists of liquid ethanol inclusions embedded in the silicon rubber matrix Ecoflex 00-35 (Smooth-On, Inc.). Programmable distribution of inclusions in the PCM-elastomer composite is easily achieved through 3D printing.[23] Upon heating the evaporation of the liquid ethanol leads to increasing pressure inside the inclusions and forces the inclusions to expand. Meanwhile, the rubber matrix expands due to the thermal expansion. As a consequence, we could observe an expansion of the soft composite with increasing temperature (Fig. 1A).

To quantitatively predict the thermomechanical behaviors of the soft composites due to liquid–vapor transition and thermal expansion, we build a micromechanics model, assuming that the ethanol inclusions in the composites are spherical and identical with uniform spatial distribution, and the silicon rubber matrix behaves within the bounds of linear elasticity. The process of liquid–vapor transition in the inclusions is described by the saturated vapor pressure ($p(T)$).[24] As ethanol in the inclusions has negligible moduli,[25] the soft composite can be treated as a porous material with internal pressure $\delta p = p(T) - p(T_0)$ applied on the voids. Based on the classical micromechanical method,[26] we obtain the effective Young's modulus E_e of the soft composite (see details in Supplementary Data)

$$\frac{E_e}{E} = \frac{4(1-f)(9\kappa+8\mu)(3\kappa+\mu)}{4(9\kappa+8\mu)(3\kappa+\mu)+f(33\kappa+56\mu)}, \quad (1)$$

where f is the volume fraction of ethanol inclusions at the reference state ($T = T_0$ in Fig. 1A). $\kappa = 423$ kPa, $\mu = 21.6$ kPa[27], and $E = 9\kappa\mu/(3\kappa+\mu)$ denote the bulk, the shear, and the Young's modulus of the elastomer matrix, respectively. As an intrinsic property measuring the resistance of the porous matrix to being deformed elastically, the effective Young's modulus of the PCM-elastomer composite above boiling temperature of ethanol is irrelative to δp, consistent with our measurement in the desired experimental strain range (Fig. 1C).[28] The effective coefficient of thermal expansion (CTE) α_e of the PCM-elastomer composite is temperature dependent owning to the presence of temperature-dependent ethanol vapor pressure and can be derived based on micromechanics analysis (see details in Supplementary Data)

$$\alpha_e = \frac{\kappa - \kappa_e}{3\kappa\kappa_e}\frac{\delta p}{\Delta T} + \alpha = \frac{3\kappa+4\mu}{12\kappa\mu}\frac{f}{1-f}\frac{\delta p}{\Delta T} + \alpha, \quad (2a)$$

and satisfies the modified Levin's formula with the presence of the internal pressure δp

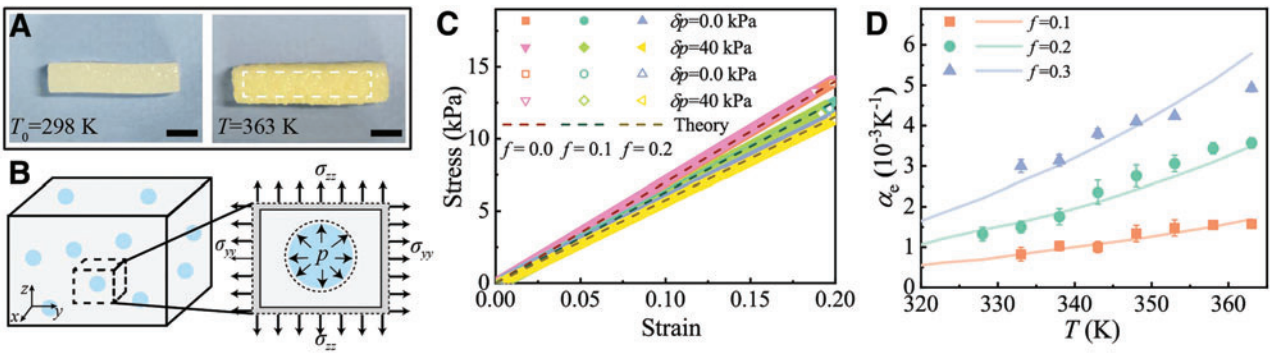

FIG. 1. Thermomechanical properties of PCM-elastomer (ethanol-silicone here) composites. **(A)** Thermal expansion of the soft composite upon temperature change from 298 K to 363 K. The volume fraction f of ethanol inclusions embedded in the silicone matrix is around 0.2. The dashed line in the right panel is the outline of the composite at $T = T_0$. Scale bars: 5 mm. **(B)** Schematic diagram for the micromechanics model of the soft composite. **(C)** Strain–stress curves of soft composites with different inclusion volume fractions ($f = 0.0$, 0.1, and 0.2) and internal vapor pressures ($\delta p = 0$ and 40 kPa) in uniaxial tension testing. *Solid* and *open symbols* are experimental data under uniaxial extension and compression, respectively. *Dashed lines* are theoretical predictions by Equation (1). **(D)** The effective CTE of the soft composite at $f = 0.1$, 0.2, and 0.3. *Symbols* are experimental data, and *solid lines* denote theoretical predictions from Equation (2). PCM, phase change material. Color images are available online.

$$\frac{3\alpha\kappa\Delta T-\delta p}{\kappa}=\frac{3\alpha_e\kappa_e\Delta T-f\delta p-3(1-f)\alpha\kappa\Delta T}{\kappa_e-(1-f)\kappa}. \quad (2b)$$

Equation (2b) relates the effective bulk moduli κ_e to the effective CTE in the presence of δp and reduces to the classical Levin's formula for materials with spherical voids at $\delta p=0$.[29,30] Here $\alpha=0.00028$ K^{-1} is CTE of the matrix at room temperature,[31] and $\Delta T=T-T_0$ is the temperature variance. The effective CTE α_e and thermal expansion $\alpha_e\Delta T$, plotted in Figure 1D and Supplementary Figure S1A, respectively, agree well with our experimental results and validate the estimation of liquid–vapor transition based on saturated vapor pressure. During the expansion for the limiting case of $f=0.3$ at $T=363$ K (Fig. 1D), the ethanol inclusions embedded in the silicon rubber matrix undergo anisotropic finite deformation, which is no longer consistent with the assumption of the spherical inclusion shape in the micromechanical theory adopted here. Therefore, the deviation between the theoretical prediction and experimental data as expected is observed at $f=0.3$ and $T=363$ K.

Supplementary Figure S1B shows that the liquid–gas transition of ethanol inclusions significantly enhances the thermal expansion of the soft composite in the presence of δp. Controlling the variance of pressure to temperature ($\delta p/\Delta T$) based on Equation (2), CTE of the soft composite is programmable and can be tuned to be zero at a critical value $(\delta p/\Delta T)_c=-12(1-f)\kappa\mu\alpha/[f(3\kappa+4\mu)]$ or even negative at $\delta p/\Delta T<(\delta p/\Delta T)_c$. Besides, the induced output stress of the soft composite is $3\kappa_e\alpha_e\Delta T=3\kappa\alpha\Delta T+[f(3\kappa+4\mu)/(3f\kappa+4\mu)](\delta p-3\kappa\alpha\Delta T)$, with $[f(3\kappa+4\mu)/(3f\kappa+4\mu)](\delta p-3\kappa\alpha\Delta T)$ as the contribution of vapor pressure. By adjusting $\delta p/\Delta T$, stress induced by vapor pressure can be designed to meet the carrying needs for the soft composites. The theoretical analysis well predicts the thermomechanical behaviors for the PCM-elastomer composites, and the estimated properties serve as fundamental implements in the finite element analysis on the deformation and locomotion of more complex structures with PCMs as shown in the following parts.

Bending of straight bilayer structures with PCM-elastomer composites

The ethanol-silicone composites with a relatively high effective CTE α_e can be utilized as thermally active structural components to trigger desired motion. Here we fabricate straight bilayer structures consisting of an active layer [ethanol-silicone elastomer composite with CTE $\alpha_2=\alpha_e$ in Eq. (2)] and a pure silicone elastomer (Ecoflex 00-30 or PDMS) with a relatively low CTE α_1 as the passive layer (Fig. 2A). The Young's modulus, thickness, and CTE of the passive and active layers are denoted by E_k, h_k, and α_k ($k=1, 2$), respectively. Subscripts 1 and 2 are used to identify quantities pertaining to the passive and active layers, respectively. In experiments, the bilayer structure has a width of 5 mm and length of 20 mm. Upon heating the active layer of a larger CTE than the passive layer is subjected to compression from the passive layer, and the whole structure bends toward the active layer; upon cooling the bilayer structure recovers to the straight configuration (Fig. 2A). The radius of curvature R at the interface of the bending bilayer structure is given by[32]

$$\frac{h}{R}=\frac{6mn(1+m)^2\varepsilon}{3mn(1+m)^2+(1+nm^3)(1+mn)}, \quad (3)$$

where h $(=h_1+h_2)$ is the thickness of the bilayer structure, $m=h_1/h_2$, $n=E_1/E_2$, and $\varepsilon=\int_{T_0}^{T}(\alpha_2-\alpha_1)\mathrm{d}T$ is the thermal-induced mismatch strain between the active and passive layer with $T_0=298$ K and $T=363$ K here.

As shown in Figure 2B and C, the theoretical analysis and numerical simulations on the bending deformation agree well with experimental results for a thick active layer ($h_2>1$ mm), but significantly overestimate the bending deformation at small h_2 ($h_2<1$ mm), given a total thickness $h_1+h_2=5$ mm. The discrepancy at small h_2 is owing to the nonuniform distribution of the ethanol inclusions in the matrix and the decreased volume fraction f due to the partial collapse of the

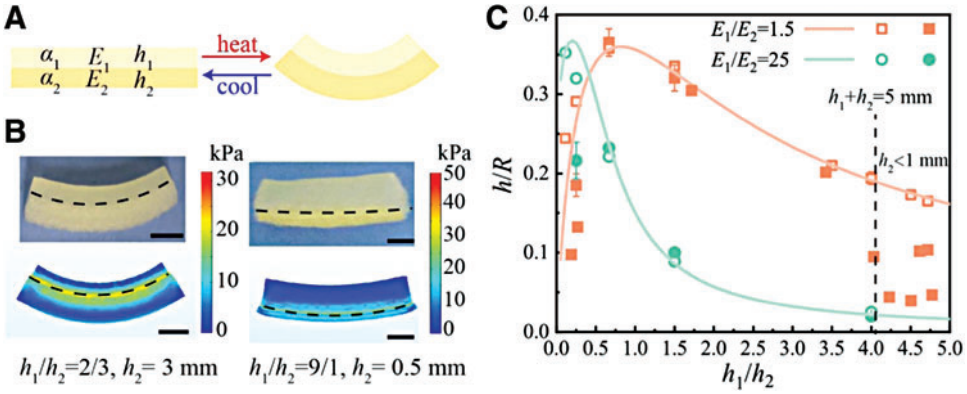

FIG. 2. Bending of temperature-response bilayer structures with phase change materials. **(A)** Illustration of the bending deformation of bilayer structure upon temperature change. *Top layer* (passive), silicon elastomer; *bottom layer* (active), silicon elastomer containing ethanol inclusions. **(B)** Experimental (*top row*) and numerical simulation (*low row*) results on the bilayer structure bending. Stress nephograms are also provided in simulations. Scale bars: 5 mm. **(C)** The normalized curvature h/R of the freestanding bilayer structure as a function of the thickness ratio h_1/h_2 ($h_1+h_2=5$ mm). *Solid symbols* are experimental data, *open symbols* are simulation results, and *solid lines* denote theoretical prediction from Equation (3). Color images are available online.

inclusions. Thickness larger than inclusion size (0.5 mm) is necessary for a designed performance of vapor pressure in PCM-elastomer matrix composites. In comparison with PDMS ($E_1/E_2 = 25$), the bilayer structure with Ecoflex 00-30 as the passive layer ($E_1/E_2 = 1.5$) at intermediate and relatively large h_1/h_2 can be actuated with larger deformation (or equivalently larger h/R in Fig. 2C). Therefore, we use Ecoflex 00-30 as the passive layer in fabricating the bilayer actuators below.

As demonstrated in Figure 2B, the bending deformation, as well as relative displacement between two ends of the initially straight structures, is relatively small. To achieve more powerful soft functioning, we propose two new design strategies, curved bilayer structures and self-folding structures, which enable the soft structures to maintain and deliver large deformation for functional use of soft actuators and robots. In the following discussion, the width w for all fabricated soft structures is 10 mm, and the volume fraction of ethanol inclusions in the ethanol-silicone elastomer composite layer is $f = 0.2$.

The ethanol could run out upon repeated heating due to the nanoporous structure of the silicon rubber matrix. Previous work in literature demonstrates that the rejuvenation of ethanol in the phase change composites could be achieved by immersing the composites into the ethanol solution. After restoring the ethanol in the PCM-elastomer composites, the retention of the original functionality of the composites could be observed.[18] PCM-elastomer composites in this work are reusable unless unexpected heat damage occurs due to repeated heating, and all designed soft robotics here can be actuated repeatedly using this repeatable rejuvenation method.

Design and characterization of soft curved bilayer structures

Similar to the straight bilayer structure discussed above, the curved bilayer structure also consists of a passive layer (pure silicone elastomer) and an active layer (ethanol-silicone elastomer composite). As shown in Figure 3A and Supplementary Figure S3A, the soft curved bilayer structure has an initial radius R_0 and an open angle $2\theta_0$ ($2\theta_0 < \pi$). Upon heating the curved structure bends with the open angle changing from $2\theta_0$ to $2\theta_f$ and the radius of curvature changing from R_0 to R_f. The initial distance between two ends of the curved structure changes from L_0 in the initial configuration to $L_0 - \Delta$ after deformation, where Δ denotes the end distance change (Fig. 3A).

The structure deformation can be estimated using the Euler–Bernoulli beam theory or linear elasticity formulation (see details in Supplementary Data). In general, the Euler–Bernoulli beam theory is more appropriate for a thin beam structure, while the linear elasticity formulation is not limited to a thin beam. As shown in Supplementary Figure S3B and C, the theoretical prediction based on the Euler–Bernoulli beam theory exhibits very small difference with that based on the linear elasticity formulation when the initial radius of the curved structure is significantly larger than its thickness ($R_0/h > 5$). In other cases, linear elasticity formulation is preferred for its good accuracy. Since there is no penetration allowed between the two ends of the curved beam, the open angle of deformed beam is required to meet $\theta_f \geq 0$. According to Equation (S15b) in Supplementary Data, the initial open angle falls in a range of

$$\frac{R_0\Delta\rho}{1+R_0\Delta\rho}\pi \leq \theta_0 < \pi \tag{4}$$

with $\Delta\rho$ given by Equation (S14b) in Supplementary Data.

The relative displacement Δ/L_0 based on geometrical relationship can be determined as

$$\frac{\Delta}{L_0} = 1 - \frac{[R_f + h_2(1+\varepsilon_2)]\sin\theta_f}{(R_0+h_2)\sin\theta_0} \tag{5}$$

with R_f and θ_f given by Euler–Bernoulli beam theory through Equation (S15) or by linear elasticity formulation through Equation (S21) in Supplementary Data. The thickness of the bilayer structure is $h = h_1 + h_2 = 5$ mm. The initial distance between two ends of the straight bilayer structure is L_0. When the passive layer contacts with the substrate, the relative displacement Δ/L_0 is expressed as

$$\frac{\Delta}{L_0} = 1 - \frac{[R_f - h_1(1+\varepsilon_1)]\sin\theta_f}{L_0} \tag{6}$$

with $R_f = R$ given in Equation (3) and $\theta_f = L_0/(2R_f)$. Here the strain associated with thermal expansion are $\varepsilon_1 = \int_{T_0}^{T} \alpha_1 dT$ and

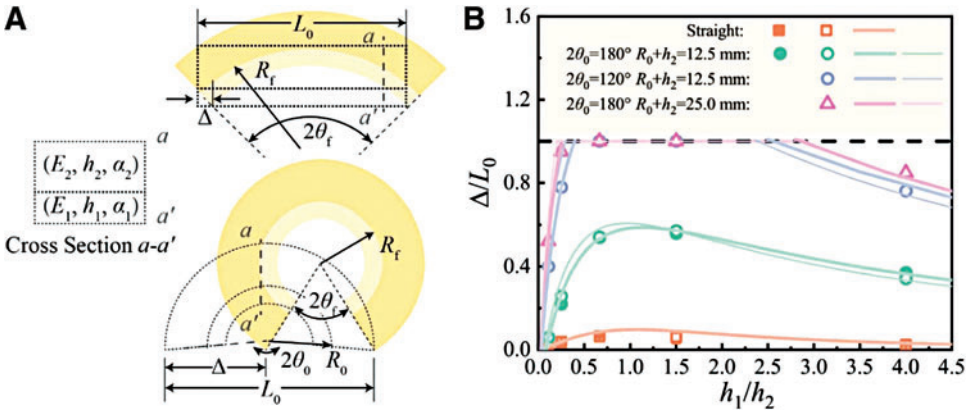

FIG. 3. Deformation of curved bilayer structures. **(A)** Illustration of the bending of the curved bilayer structures. **(B)** The relative displacement Δ/L_0 of two structure ends under fixed thickness ($h_1 + h_2 = 5$ mm) as a function of the thickness ratio h_1/h_2. *Solid points* are experimental data, *hollow points* are simulation results. *Thick* and *thin lines* are theoretical predictions based on the Euler–Bernoulli beam theory and linear elasticity, respectively. Color images are available online.

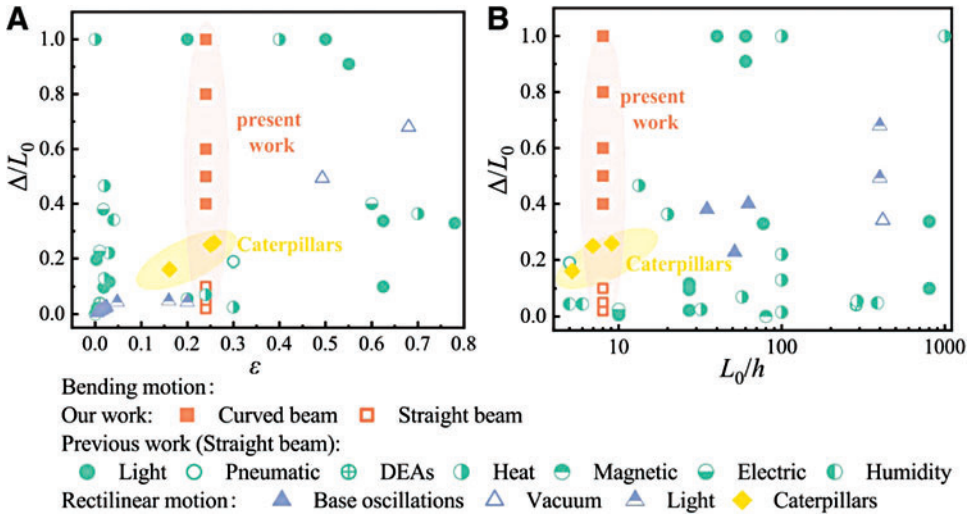

FIG. 4. Summary of relative deformation of soft structures. Δ/L_0 versus **(A)** mismatched strain ε and **(B)** the normalized structure length L_0/h with h as the total thickness of the structure. The *orange squares* (*solid* for curved structures and open for straight structures) are the results of present work. Data (see Supplementary Table S1) are referred to references in Supplementary Data. Color images are available online.

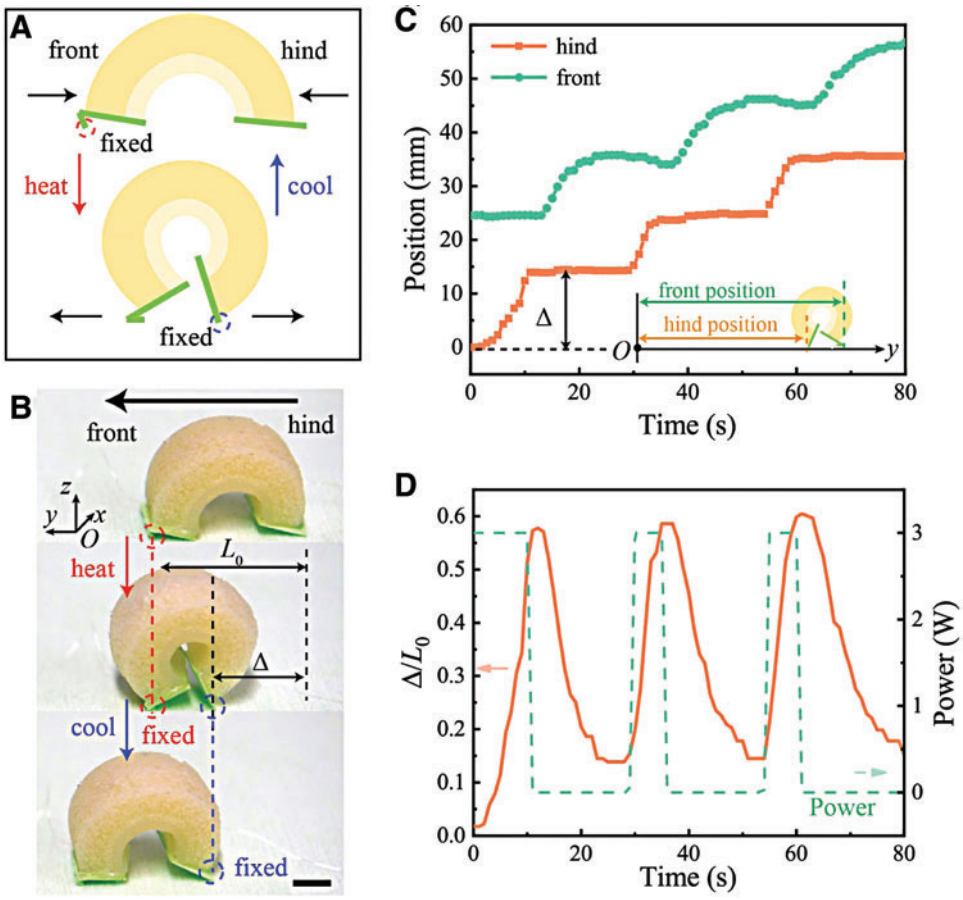

FIG. 5. Characterization of crawling inchworm robots during heating–cooling cycles. **(A)** Illustration of the locomotion due to the difference in friction between the two ends and the substrate surface. **(B)** Crawling of the inchworm robot in one heating–cooling cycle with an end displacement Δ. The front end remains stationary and the hind end slides forward upon heating, while the hind end stays with the front end sliding forward upon cooling. Heating and cooling are electrically controlled by the embedded resistance wire. Scale bar: 5 mm. **(C)** Temporal evolution of the position of the inchworm robot's front and hind ends (shown as the inset). The platform of the curve corresponds to the stationary state of two ends. **(D)** Temporal evolution of the relative displacement Δ/L_0 of the inchworm robot. The *dashed line* is the temporal variation of the input power in the embedded resistance wire. Color images are available online.

$\varepsilon_2 = \int_{T_0}^{T} \alpha_2 dT$. Figure 3B shows that the relative displacement Δ/L_0 significantly depends on the open angle $2\theta_0$ and the radius of curvature R_0 and varies in a full range from 0 to 1 by adjusting θ_0 and R_0. The smaller θ_0 or the larger R_0 is, the larger Δ/L_0 is. At $\Delta/L_0 = 1$, two bilayer ends come into contact. Figure 4 compares the relative deformation of soft structures in literature and present work. It is shown that our design of the curved bilayer structures with PCMs could achieve a large relative displacement at a mismatch strain ε around 0.24 (Fig. 4A). Moreover, the curved bilayer design is suitable for the thick structures with a relatively large h (Fig. 4B).

Design of inchworm robot and its locomotion under controlled heating

The mechanical analysis above indicates that thick curved bilayer structures with PCMs powered by temperature variation can generate relatively large motion without a significant loss of rigidity. Based on this feature, we design and fabricate inchworm robots, which are capable of multimodal locomotion with object carrying. Figure 5A illustrates the design of the inchworm robot where a resistance wire is embedded in the active layer to achieve electrical control of heating and cooling (see Materials Fabrication and Testing section in Supplementary Data and Supplementary Fig. S4). The curved bilayer structure has an initial radius $R_0 = 9.5$ mm, total thickness $h = 5$ mm with active layer thickness 3 mm, and initial angle $2\theta_0 = 180°$.

As shown in Figure 5A, the hind (right) end of the bilayer is attached with a flat sheet and on the front (left) end there is a small tip on the attached sheet. Due to the large end displacement and open angle change, the sheet edges, as well as the tip surface and edge, can form contact with the substrate surface. Upon heating the bilayer structure becomes more upward convex. Owing to the two edges connecting with the substrate, the front end has a larger coefficient of static friction than the hind end with one contact edge.[33–35] Therefore, during heating the hind end slides forward (leftward here), while the front end stands and rotates around the tip edge. Upon cooling the bilayer structure tends to return to the initial less upward convex configuration and spreads two ends. As the sheet attached on the hind end rotates more, the friction force on the hind end is larger than that on the front end. As a consequence, the front end slides forward while the hind end is fixed. During the heating–cooling cycles, a unidirectional locomotion of the inchworm robot is achieved as shown in Figure 5B and Supplementary Movie M1. Temporal evolution of the position of the front and hind ends and relative displacement Δ/L_0 are plotted in Figure 5C and D. In one heating–cooling cycle, the inchworm robot can achieve a relative displacement $\Delta = 0.6L_0$, which fits the result in Figure 3B. The speed of the moving inchworm robot is about 0.75 mm/s (0.03 body length/s), a medium speed level among artificial soft robots.[33]

To demonstrate the carrying capacity of the inchworm robot, we put metal blocks on the robot and monitored its crawling (Fig. 6 and Supplementary Movie M2). The load

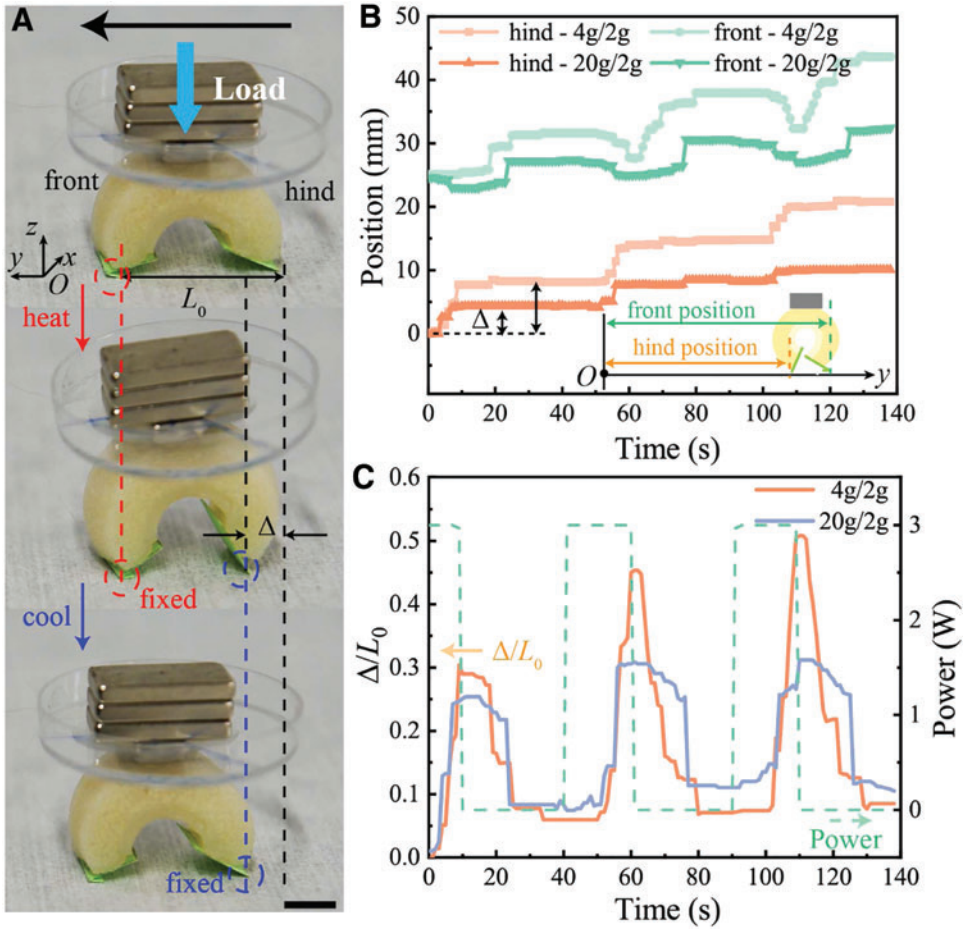

FIG. 6. Inchworm robots crawling and carrying objects. **(A)** Crawling of the object-loaded inchworm robot (robot itself 2 g, load 20 g) in one heating–cooling cycle with a displacement Δ. Scale bar: 5 mm. **(B)** Temporal evolution of the position of the inchworm actuator's front and hind ends under different loads (4 and 20 g). **(C)** Temporal evolution of the relative displacement Δ/L_0 (*solid lines*) at different loads (4 and 20 g) in response to the input power (*dashed line*). Color images are available online.

affects the friction between the robot and substrate, leading to a decrease of the displacement Δ and the crawling speed in each heating–cooling cycle (Fig. 6B, C). The heavier the load is, the slower the robot locomotion is. The robot carrying 4 g load achieves $\Delta/L_0 = 0.45$ in one heating–cooling cycle, while $\Delta/L_0 = 0.3$ at 20 g load (Fig. 6C). The speed of the crawling inchworm robot at 4 g load is about 0.23 mm/s, while at 20 g load the speed is about 0.15 mm/s. Owing to the thick layer structure, the movement of the inchworm robot with heavy load (10 times its own weight) is stable and repeatable without tumbling. As the load is heavier than 25 g, the robot falls over due to the high center of gravity.

Assembling two inchworm robots in parallel,[36,37] a two-part inchworm robot is fabricated with the capacity of multimodal locomotion such as crawling and taking turn by individual control of each inchworm part (Fig. 7 and Supplementary Movie M3). At the same input power, two parts of the inchworm robot move at the same pace and the robot as a whole crawl in a straight path. The inchworm robot can also take turn with a difference in the input power between two parts. A 90° turn can be easily achieved by the asymmetry deformation of the two parts of the inchworm robot.

Design and fabrication of soft grippers with PCMs

The thick curved bilayer structure can also be used in the design of soft grippers (Fig. 8). Different from traditional grippers,[38] the soft gripper here is composed by n identical units, each consisting of a curved bilayer structure with PCMs and a connector connecting two neighboring gripper fingers (Fig. 8A). The curved bilayer structure has an initial radius of 9.5 mm, thickness of 5 mm (thickness ratio $h_1/h_2 = 2/3$), and the connector has the length of 12 mm and thickness of 2 mm. $2\theta_0 = 180°–360°/n$ is the initial open angle of the bilayer structure. The soft gripper is annular, and there is an inscribed circular region with radius R_{in} in the center. The grabbing is achieved by the shrinking of the gripper upon heating with the angle change from $2\theta_0$ to $2\theta_d$ and the radius change from R_{in} to R_d.

Figure 8B shows the simulation results on the shrinking of the grippers ($n = 3$, 4, 5, and 6). In the simulations, the parameters of the passive layer are $\kappa_1 = 423$ kPa, $\mu_1 = 21.6$ kPa,[27] and $\alpha_1 = 0.00028$ K^{-1},[31] and those of the active layer are $\kappa_2 = \kappa_e$, $\mu_2 = \mu_e$ [Eq. (S4) in Supplementary Data], and $\alpha_2 = \alpha_e$ [Eq. (2)], with temperature change from $T_0 = 298$ K to $T = 363$ K. Figure 8C indicates the relative shrinking degree characterized by R_d/R_{in} describing the adaptability of the gripper to different object sizes. As n increases, R_d/R_{in} increases. At $n = 5$, the shrinking of the gripper ranges from $0.5R_{in}$ to R_{in} (Fig. 8C), which is large enough for the grasping of a strawberry and a small glass bottle (Fig. 8D and Supplementary Movie M4).

The object grasped by the soft gripper forms contact with the connectors, which are composed of silicone rubber without embedded resistance wires here. The temperature of

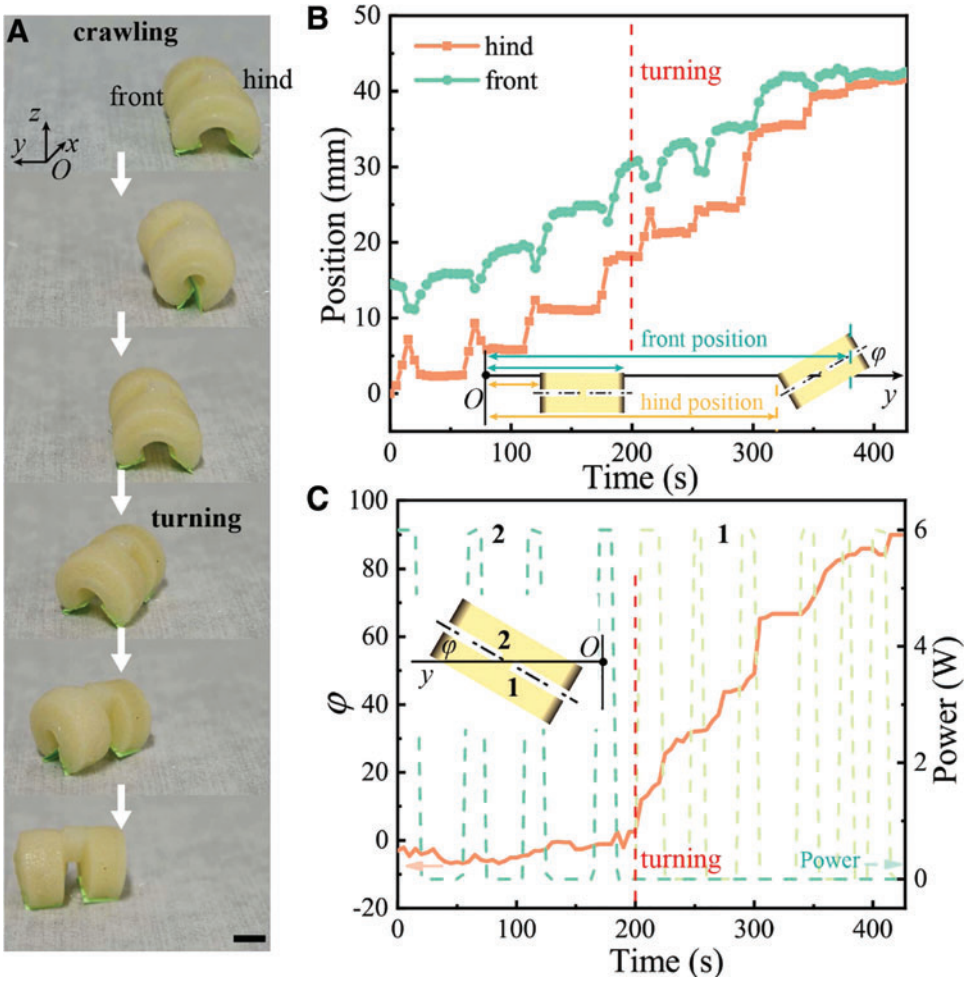

FIG. 7. Multimodal locomotion of a two-part inchworm robot. **(A)** Crawling and turning locomotion modes. Scale bar: 5 mm. **(B)** Temporal evolution of the front and hind ends of the two-part inchworm robot (shown as the inset). **(C)** Temporal evolution of angle φ (*solid line*) of robot turning in response to the input power (*dashed lines*). φ is the angle between the initial moving direction and the current moving direction. Color images are available online.

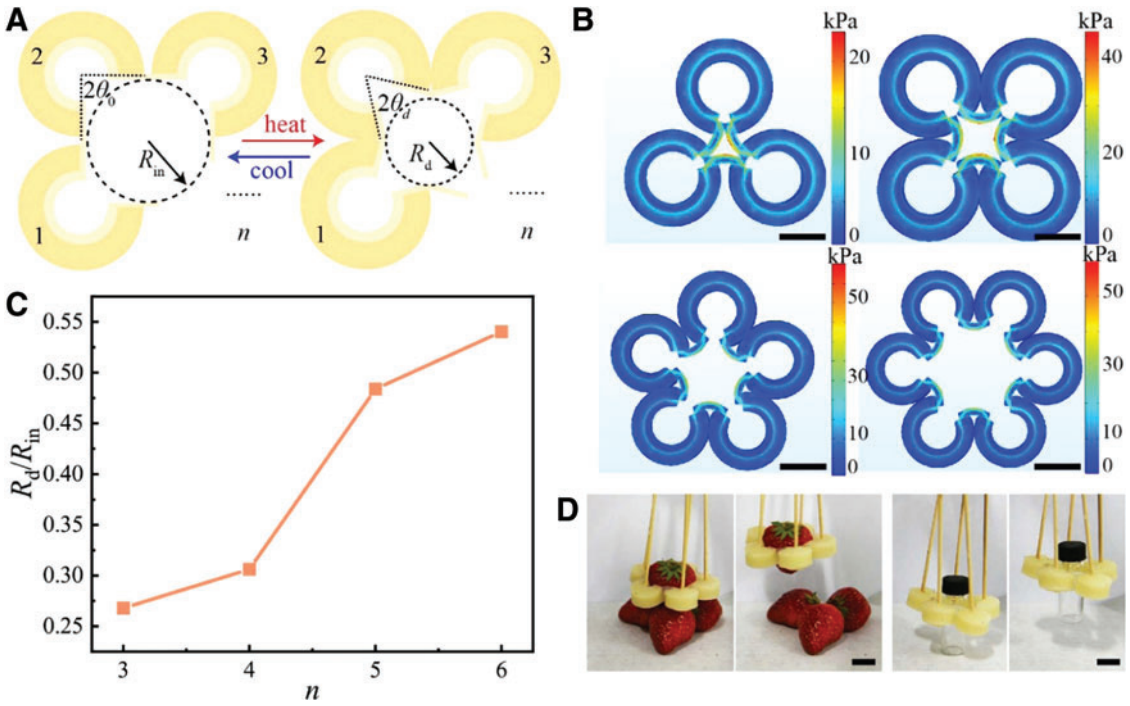

FIG. 8. Design of soft grippers and grabbing demonstration. **(A)** Illustration of the gripper design. The gripper is made up of n identical units, each unit consisting of a curved bilayer structure and a connector. **(B)** The stress nephogram of the deformed grippers and **(C)** corresponding relative shrinking degrees R_d/R_{in} in numerical simulations when two ends of each gripper unit form contact. Scale bars: 1 cm. **(D)** Grabbing the strawberry and bottle by the gripper with five units. Scale bars: 1 cm. Color images are available online.

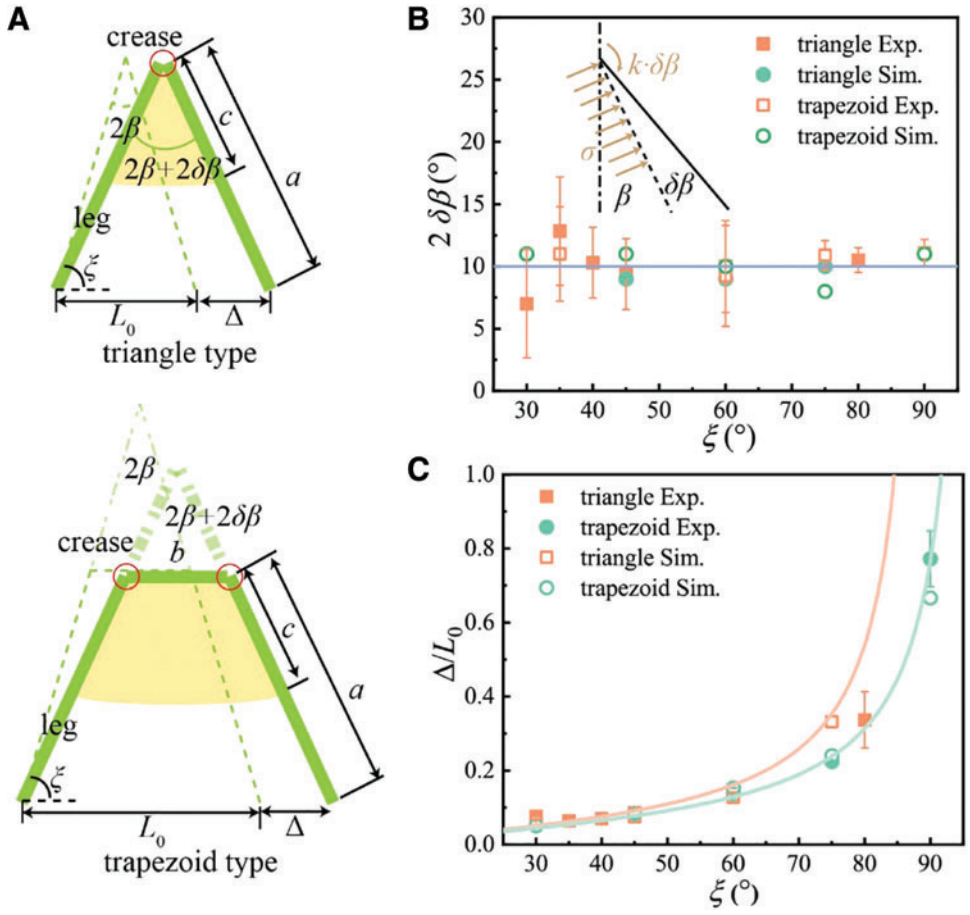

FIG. 9. Design and characterization of self-folding structures with PCM-based joint actuators. **(A)** Design of the self-folding structures. Creases shown in *red circle* are cuts with fixed cutting depths. The PCM–elastomer composite serves as the actuator beneath the creases. **(B)** The top angle changes $2\delta\beta$ as a function of the initial side angle ξ, which is around 10° here. **(C)** The relative displacement Δ/L_0 as a function of ξ. *Solid symbols* are experimental data, *open symbols* denote simulation results, and *solid lines* are theoretical prediction [Equation (7)]. Color images are available online.

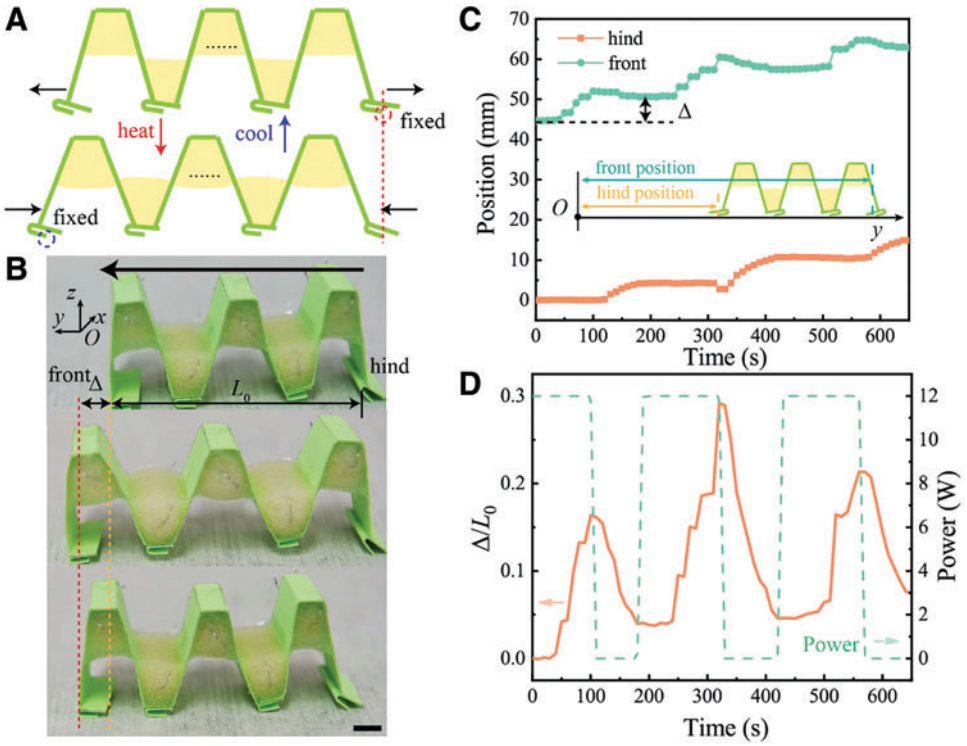

FIG. 10. Multi self-folding structures with soft PCM-based joint actuators. **(A)** Illustration of the assembly into a worm-like soft robot. **(B)** Crawling of the assembly in one heating–cooling cycle with a displacement of Δ. Scale bar: 5 mm. **(C)** Temporal evolution of the position of the front and hind ends of the multi self-folding structures (shown as the inset). **(D)** Temporal evolution of the relative displacement Δ/L_0 (*solid lines*) in response to the input power (*dashed line*). Color images are available online.

the connector depends on its heat exchanging with the phase change composite, which is not evident as the thermal conductivity of silicone rubber is low (0.2 W/mK).[39] Therefore, there is no heat damage observed on the grasped object (e.g., the strawberry and bottle in Fig. 8D).

Self-folding structures with PCMs

Thermally active soft joint actuators are another interesting implication of the PCM-based soft composites.[40] As shown in Figure 9, we fabricate self-folding structures composed of two or three stiff sheets linked together with one or two folds (or creases). Between two long legs there is a soft joint actuator made of the PCM-based soft composite. The self-folding structure has an initial top angle 2β and a side angle $\xi = (\pi - 2\beta)/2$. The leg length is $a = 20$ mm, and the thickness of the soft composite is $c = 10$ mm. The trapezoid type structure has a top sheet of width $b = 5$ mm. Upon heating the soft composite expands, resulting in a spreading of the robot legs with a top angle increase of $2\delta\beta$; upon cooling the soft composite tends to return to the initial configuration with a decrease of the top angle. The crease subject to folding can be modeled as a spiral spring of stiffness k[41,42] and the increase of the top angle is $2\delta\beta = 2\sigma c/k$ with σ as the blocked stress induced by the soft joint deformation (see details in Supplementary Data and Supplementary Fig. S2). In our experiments, $2\delta\beta$ is around 10° (Fig. 9B). The corresponding relative displacement Δ/L_0 is given from the geometrical relation as

$$\frac{\Delta}{L_0} = \begin{cases} \frac{\cos(\xi - \delta\beta)}{\cos\xi} - 1, & \text{triangle type,} \\ \frac{2a\cos(\xi - \delta\beta) + b}{2a\cos\xi + b} - 1, & \text{trapezoid type.} \end{cases} \quad (7)$$

It is shown that Δ/L_0 strongly depends on the side angle ξ (Fig. 9C). Structures with a large ξ exhibit a large displacement Δ/L_0.

By attaching tips beneath the front and hind legs of the self-folding structure, the structure can achieve unidirectional crawling at a speed around 0.10 mm/s as shown in Supplementary Figure S6 and Supplementary Movie M5. The underlying mechanism is similar to that governing the crawling of inchworm robots in Figure 5. By repeating the heating–cooling cycle, the self-folding structures with attached tips achieve a push–pull locomotion. The self-folding structures are readily assembled into complex structure. Figure 10 shows an assembly of the self-folding structures into a worm-like soft robot by end-to-end linking. In one thermal cycle, the assembled structure with a side angle $\xi = 80°$ moves with $\Delta = 0.2L_0$, consistent with the result in Figure 9C. The corresponding speed is 0.05 mm/s.

Conclusions

PCM-elastomer composites as attractive actuating components in forming advanced soft composites for robotic applications are facing the problem of less understanding of their thermomechanical properties, which in turn limits the rational design for engineering structures. Here we study the effective thermomechanical properties of the PCM-elastomer composites using the micromechanical theory and reveal how the vapor pressure in the PCM inclusions strengthens the composite expansion and output stress. Bilayer structures with programmable deformability are designed by controlling the inclusion distribution and contents. Complex locomotion and adaptable grapping are achieved through the assembly of deformable cells with asymmetrical friction and deformation. The results expand the functionality and

application of the PCM-elastomer composites capable of adaptable deformation and multimode locomotion.

Author Disclosure Statement

No competing financial interests exist.

Funding Information

Financial support for this work was provided by the National Natural Science Foundation of China under Grant Nos. 91848201, 11988102, 11521202, 11872004, 11802004 and the Young Elite Scientists Sponsorship Program by the China Association for Science and Technology under Grant 2017QNRC001.

Supplementary Material

Supplementary Data
Supplementary Figure S1
Supplementary Figure S2
Supplementary Figure S3
Supplementary Figure S4
Supplementary Figure S5
Supplementary Figure S6
Supplementary Table S1
Supplementary Movie M1
Supplementary Movie M2
Supplementary Movie M3
Supplementary Movie M4
Supplementary Movie M5

References

1. Rus D, Tolley MT. Design, fabrication and control of soft robots. Nature 2015;521:467–475.
2. Chiolerio A, Quadrelli MB. Smart fluid systems: the advent of autonomous liquid robotics. Adv Sci 2017;4:1700036.
3. Majidi C. Soft robotics: a perspective-current trends and prospects for the future. Soft Robot 2014;1:5–11.
4. Zou W, Jin B, Wu Y, *et al.* Light-triggered topological programmability in a dynamic covalent polymer network. Sci Adv 2020;6:eaaz2362.
5. Zheng SY, Shen Y, Zhu F, *et al.* Programmed deformations of 3D-printed tough physical hydrogels with high response speed and large output force. Adv Funct Mater 2018;28: 1803366.
6. Cao CJ, Hill TL, Conn AT, *et al.* Nonlinear dynamics of a magnetically coupled dielectric elastomer actuator. Phys Rev Appl 2019;12:044033.
7. Lendlein A. Fabrication of reprogrammable shape-memory polymer actuators for robotics. Sci Robot 2018;3:eaat9090.
8. Hines L, Petersen K, Lum GZ, *et al.* Soft actuators for small-scale robotics. Adv Mater 2017;29:1603483.
9. Wong WSY, Li M, Nisbet DR, *et al.* Mimosa origami: a nanostructure-enabled directional self-organization regime of materials. Sci Adv 2016;2:e1600417.
10. Palagi S, Mark AG, Reigh SY, *et al.* Structured light enables biomimetic swimming and versatile locomotion of photoresponsive soft microrobots. Nat Mater 2016;15:647–653.
11. Al-Rubaiai M, Pinto T, Qian C, *et al.* Soft actuators with stiffness and shape modulation using 3D-printed conductive polylactic acid material. Soft Robot 2019;6:318–332.
12. Ma P, Niu B, Lin J, *et al.* Sequentially controlled deformations of patterned hydrogels into 3D configurations with multilevel structures. Macromol Rapid Commun 2019;40:1800681.
13. Song GE, Kim KH, Lee YP. Simulation and experiments for a phase-change actuator with bistable membrane. Sens Actuators A 2007;136:665–672.
14. An S, Kang DJ, Yarin AL. A blister-like soft nano-textured thermo-pneumatic actuator as an artificial muscle. Nanoscale 2018;10:16591–16600.
15. Nishikawa Y, Matsumoto M. A design of fully soft robot actuated by gas-liquid phase change. Adv Robot 2019;33: 567–575.
16. Han J, Jiang W, Niu D, *et al.* Untethered soft actuators by liquid-vapor phase transition: remote and programmable actuation. Adv Intell Sys 2019;8:1900109.
17. Miriyev A, Stack K, Lipson H. Soft material for soft actuators. Nat Commun 2017;8:596.
18. Miriyev A, Trujillo C, Caires G, *et al.* Rejuvenation of soft material-actuator. MRS Commun 2018;8:556–561.
19. Li S, Vogt DM, Rus D, *et al.* Fluid-driven origami-inspired artificial muscles. Proc Natl Acad Sci USA 2017;114: 13132–13137.
20. Chellattoan R, Yudhanto A, Lubineau G. Low-voltage-driven large-amplitude soft actuators based on phase transition. Soft Robot 2020. DOI: 10.1089/soro.2019.0150
21. Lee JG, Rodrigue H. Origami-based vacuum pneumatic artificial muscles with large contraction ratios. Soft Robot 2019;6:109–117.
22. Zhou Z, Li Q, Chen L, *et al.* A large-deformation phase transition electrothermal actuator based on carbon nanotube-elastomer composites. J Mater Chem B 2016;4:1228–1234.
23. Li X, Zhang JM, Yi X, *et al.* Multimaterial microfluidic 3D printing of textured composites with liquid inclusions. Adv Sci 2019;6:1800730.
24. Dillon HE, Penoncello SG. A fundamental equation for calculation of the thermodynamic properties of ethanol. Int J Thermophys 2004;25:321–335.
25. Chen X, Li M, Yang M, *et al.* The elastic fields of a compressible liquid inclusion. Extreme Mech Lett 2018;22:122–130.
26. Duan HL, Wang J, Huang ZP, *et al.* Size-dependent effective elastic constants of solids containing nano-inhomogeneities with interface stress. J Mech Phys Solids 2005;53:1574–1596.
27. Overvelde JTB, Dykstra DMJ, de Rooij R, *et al.* Tensile instability in a thick elastic body. Phys Rev Lett 2016;117: 094301.
28. Krichen S, Liu L, Sharma P. Liquid inclusions in soft materials: capillary effect, mechanical stiffening and enhanced electromechanical response. J Mech Phys Solids 2019;127:332–357.
29. Levin VM. Thermal expansion coefficients of heterogeneous materials. Mech Solids 1967;2:58–61.
30. Duan HL, Karihaloo BL. Thermo-elastic properties of heterogeneous materials with imperfect interfaces: generalized Levin's formula and Hill's connections. J Mech Phys Solids 2007;55:1036–1052.
31. Lee TI, Kim MS, Kim TS. Contact-free thermal expansion measurement of very soft elastomers using digital image correlation. Polym Test 2016;51:181–189.
32. Timoshenko S. Analysis of bi-metal thermostats. J Opt Soc Am 1925;11:233–255.
33. Shin B, Ha J, Lee M, *et al.* Hygrobot: a self-locomotive ratcheted actuator powered by environmental humidity. Sci Robot 2018;3:eaar2629.

34. Rafsanjani A, Zhang Y, Liu B, *et al.* Kirigami skins make a simple soft actuator crawl. Sci Robot 2018;3:eaar7555.
35. Yamaguchi T, Sawae Y, Rubinstein SM. Effects of loading angles on stick-slip dynamics of soft sliders. Extreme Mech Lett 2016;9:331–335.
36. Qin L, Liang X, Huang H, *et al.* A versatile soft crawling robot with rapid locomotion. Soft Robot 2019;6:455–467.
37. Gu G, Zou J, Zhao R, *et al.* Soft wall-climbing robots. Sci Robot 2018;3:eaat2874.
38. Shintake J, Cacucciolo V, Floreano D, *et al.* Soft robotic grippers. Adv Mater 2018;30:1707035.
39. Bartlett MD, Kazem N, Powell-Palm MJ, *et al.* High thermal conductivity in soft elastomers with elongated liquid metal inclusions. Proc Natl Acad Sci USA 2017;114: 2143–2148.
40. Zhao J, Zhang J, McCoul D, *et al.* Soft and fast hopping-running robot with speed of six times its body length per second. Soft Robot 2019;6:713–721.
41. Santangelo CD. Extreme mechanics: self-folding origami. Annu Rev Condens Matter Phys 2017;8:165–183.
42. Waitukaitis S, Menaut R, Chen BG, *et al.* Origami multi-stability: from single vertices to metasheets. Phys Rev Lett 2015;114:055503.

Address correspondence to:
Xin Yi
State Key Laboratory for Turbulence and Complex Systems
Department of Mechanics and Engineering Science
BIC-ESAT
College of Engineering
Peking University
Beijing 100871
China

E-mail: xyi@pku.edu.cn

Pengyu Lv
State Key Laboratory for Turbulence and Complex Systems
Department of Mechanics and Engineering Science
BIC-ESAT
College of Engineering
Peking University
Beijing 100871
China

E-mail: lvpy@pku.edu.cn

Supplemental Materials

Soft Actuators Based on Liquid-Vapor Phase Change Composites

Xiying Li, Huiling Duan, Pengyu Lv and Xin Yi

Supplementary Data

1. Micromechanical model of phase change materials (PCMs)-elastomer composites

To predict the deformation of the PCMs-elastomer composite (ethanol-silicone composite here) upon temperature change, the liquid-vapor transition of the ethanol inclusions is treated as an internal pressure change applied on the inclusion-matrix interface and the classical micromechanical theory is employed to derive the mechanical and thermal behaviors of the porous composite with internally pressurized spherical voids as follows.

We first determine the internal pressure upon the ethanol-silicone interface. Based on experimental data, the vapor pressure of ethanol at temperature T is given as[1]

$$p(T) = p_c \times \exp\left[\frac{T_c}{T}\left(-0.051477\theta^{1/2} - 8.27075\theta - 5.49245\theta^3 + 5.64829\theta^{11/2}\right)\right], \quad \text{(S1)}$$

where $\theta = 1 - T/T_c$. Here the critical pressure p_c = 6.15 MPa and the critical temperature T_c = 513.9 K together define ethanol's liquid-vapor critical point, which represents the end of the pressure-temperature curve in thermodynamics. Above p_c, the vapor cannot be liquefied at any pressure. At room temperature T_0, the vapor pressure p_0 inside ethanol inclusion is around 7.8 kPa, which is balanced by the deformation of the elastomer matrix. Upon heating to temperature T, the ethanol pressure increases to $p(T) = p_0 + \delta p$ and the elastomer matrix is deformed further.

Treating the silicone matrix as a linear isotropic elastic material, its strain-displacement equations, equilibrium equations, and constitutive equations are

$$\begin{aligned} &\boldsymbol{\varepsilon} = \tfrac{1}{2}(\nabla\mathbf{u} + \mathbf{u}\nabla), \\ &\nabla\cdot\boldsymbol{\sigma} = \mathbf{0}, \\ &\boldsymbol{\sigma} = \left(\kappa - \tfrac{2}{3}\mu\right)\mathrm{tr}(\boldsymbol{\varepsilon})\mathbf{I} + 2\mu\boldsymbol{\varepsilon} - 3\kappa\alpha\Delta T\mathbf{I}, \end{aligned} \quad \text{(S2)}$$

where $\boldsymbol{\varepsilon}$ and $\boldsymbol{\sigma}$ represent the strain and stress tensors, respectively. $\mathbf{u}$ is the displacement vector, and ∇ is the nabla symbol. tr($\boldsymbol{\varepsilon}$) denotes the trace of $\boldsymbol{\varepsilon}$, and $\mathbf{I}$ is the identity tensor. κ = 423 kPa and μ = 21.6 kPa are the bulk and shear moduli of the matrix, respectively.[2] α =0.00028 K^{-1} is the coefficient of thermal expansion (CTE) of the silicone matrix.[3] $\Delta T = T - T_0$ is the change in temperature. Hereinafter the state at room temperature is taken as the reference state.

To determine the effective moduli of the porous composite with internally pressurized spherical voids, we employ the Mori-Tanaka method, one of the classical micromechanical schemes,[4,5] from which we have the relation between the average stress $\bar{\boldsymbol{\sigma}}$ and average strain $\bar{\boldsymbol{\varepsilon}}$ of the composite as

$$\bar{\boldsymbol{\sigma}} = \left(\kappa_e - \tfrac{2}{3}\mu_e\right)\mathrm{tr}(\bar{\boldsymbol{\varepsilon}})\mathbf{I} + 2\mu_e\bar{\boldsymbol{\varepsilon}} - 3\kappa_e\alpha_e\Delta T\mathbf{I}, \quad \text{(S3)}$$

where κ_e and μ_e are the effective bulk and shear moduli of the porous composite, respectively, and given as[4, 5]

$$\begin{aligned} &\kappa_e = (1-f)\frac{4\mu}{3f\kappa+4\mu}\kappa, \\ &\mu_e = (1-f)\frac{9\kappa+8\mu}{9\kappa+8\mu+6f(\kappa+2\mu)}\mu, \end{aligned} \quad \text{(S4)}$$

with f as the volume fraction of the ethanol inclusions. Then the effective Young's modulus of the composite $E_e = 9\kappa_e\mu_e/(3\kappa_e+\mu_e)$ can be obtained as

$$\frac{E_e}{E}=\frac{4(1-f)(9\kappa+8\mu)(3\kappa+\mu)}{4(9\kappa+8\mu)(3\kappa+\mu)+3f\kappa(33\kappa+56\mu)}, \quad \text{(S5)}$$

where $E = 9\kappa\mu/(3\kappa+\mu)$ is the Young's modulus of the matrix. Since the internal pressure variation δp is strain-independent and can be regarded as thermal loading on the matrix, the effective modulus of the composite is independent of δp as expected and predicted in Equation S5, which is also consistent with our experimental results (Figure 1C in the main text).

Upon free thermal expansion ($\bar{\boldsymbol{\varepsilon}} = \mathrm{tr}(\bar{\boldsymbol{\varepsilon}})/3\mathbf{I}$), the average stress $\bar{\boldsymbol{\sigma}} = \int(\boldsymbol{\sigma}\cdot\mathbf{N})\otimes\mathbf{x}\mathrm{d}S$ can be expressed as $\bar{\boldsymbol{\sigma}} = (1-f)4\kappa\mu/(3f\kappa+4\mu)\mathrm{tr}(\bar{\boldsymbol{\varepsilon}})\mathbf{I} - f\delta p\mathbf{I}$ with $\mathbf{N}$ as the outward unit normal vector to the external boundary S of the representative volume element (RVE) and $\mathbf{x}$ as the position vector.[4, 5] Combined with Equation S3, the effective coefficient of thermal expansion (CTE) α_e reads

$$\alpha_e = \frac{f}{1-f}\frac{3\kappa+4\mu}{12\kappa\mu}\frac{\delta p}{\Delta T}+\alpha, \quad \text{(S6)}$$

which depends on the temperature change ΔT as confirmed by our experimental results (Figure 1D) and satisfies the following formula

$$\frac{3\alpha\kappa\Delta T-\delta p}{\kappa}=\frac{3\alpha_e\kappa_e\Delta T-f\delta p-3(1-f)\alpha\kappa\Delta T}{\kappa_e-(1-f)\kappa}. \quad \text{(S7)}$$

Equation S7, relating the effective bulk moduli to the effective CTE in the presence of δp, can be regarded as a modified Levin's formula [6, 7] for a composite with internally pressurized spherical voids. From Equation S3, the relative volume change $\bar{\varepsilon}_{kk} = \mathrm{tr}(\bar{\boldsymbol{\varepsilon}}) = (V-V_0)/V_0$ of the PCMs-elastomer composite under free expansion is

$$\frac{\bar{\varepsilon}_{kk}}{3}=\alpha_e\Delta T=\frac{f}{1-f}\frac{3\kappa+4\mu}{12\kappa\mu}\delta p+\alpha\Delta T, \quad \text{(S8)}$$

which agrees well with our experimental results in Supplementary Figure S1, and validates the estimation of the liquid-gas transition based on the saturated vapor pressure (Equation S1).

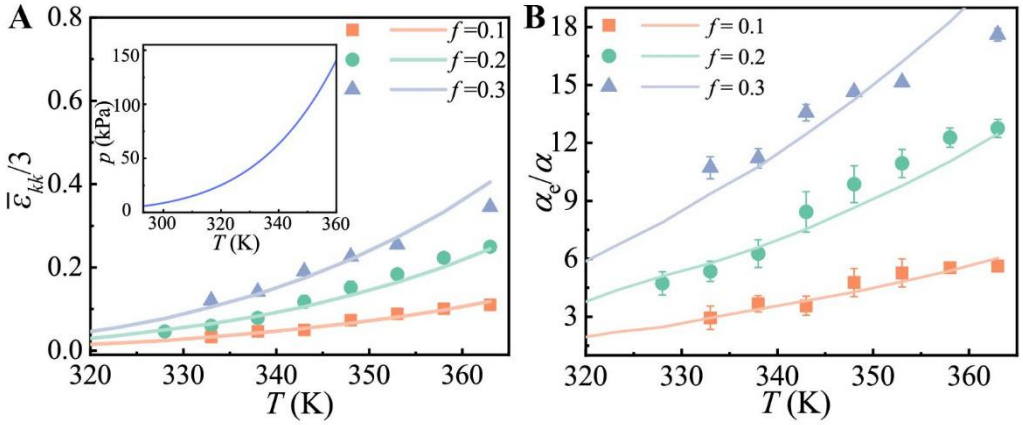

FIG. S1. Thermal expansion of the ethanol-silicon composite. **(A)** Volume change $\bar{\varepsilon}_{kk}/3$ and **(B)** CTE ratio α_e/α as a function of temperature T. Symbols are experimental data, and solid lines in **(A)** and **(B)** denote theoretical prediction given in Equations S8 and S6, respectively. Inset is the ethanol pressure p varying with temperature T.

Another interesting case is the deformation of the ethanol-silicone composite upon

a displacement constraint. Here we consider the case of uniaxial elongation of a composite confined in a rigid cylindrical tube and introduce a cylindrical coordinate $r\phi z$ with its z-axis along the cylindrical axis of the tube (Supplementary Figure S2A, inset). As shown in Supplementary Figure S5B, a cylindrical composite sample is inserted into the rigid heating tube to confine its radial expansion. Two force gauges are attached at two ends of the tube to measure the thermal stress of the composite upon heating. Upon heating, the sample first expands freely in the axial direction and then contacts with the force gauges at a sufficiently high temperature. At this moment, a prescribed axial strain $\varepsilon_0 = 1 - l_0/L$ is achieved with l_0 the initial length of the cylindrical sample and L the length of the cylindrical tube, and the constraint force is measured.

In the case of free thermal expansion along the axial direction, the boundary conditions are $\bar{\sigma}_{zz} = 0$ at two tube ends and $\bar{\varepsilon}_{rr} = 0$ at the circumferential interface between the composite and the confining tube. The free expansion in z direction with circumferential constraint from Equation S3 is characterized by

$$\bar{\varepsilon}_{zz} = \frac{3\kappa_e\alpha_e\Delta T}{\kappa_e+4\mu_e/3} = \left[1 - \frac{3f(3\kappa-4\mu)}{3(3+5f)\kappa+8\mu}\right]\frac{9\kappa}{3\kappa+4\mu}\alpha_e\Delta T, \tag{S9}$$

where α_e is given in Equation S8 and the relation between $\bar{\varepsilon}_{zz}$ and ΔT at different f is shown in Supplementary Figure S2A. In the case of a three-dimensional displacement constraint ($\bar{\varepsilon}_{zz} = \varepsilon_0$ at two tube ends and $\bar{\varepsilon}_{rr} = 0$ at the circumferential interface between the composite and the confining tube), the stress $\bar{\sigma}_{zz}$ at two ends of the cylindrical composite is

$$\bar{\sigma}_{zz} = -3\kappa_e\alpha_e\Delta T + \left(\kappa_e + \frac{4}{3}\mu_e\right)\varepsilon_0, \tag{S10}$$

where κ_e and μ_e are given in Equation S4. Our experimental results confirm the theoretical prediction given in Equation S10 as shown in Supplementary Figure S2B, where the kinks in the solid curves represent the moments the composite achieves the prescribed strain ε_0.

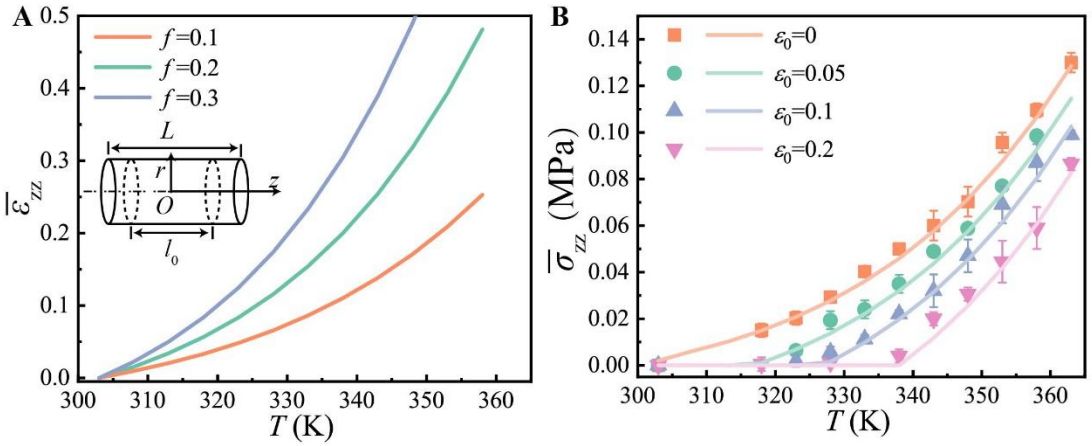

FIG. S2. Thermal expansion of radially confined ethanol-silicone composites. **(A)** Free thermal expansion along the axial direction at volume fractions f = 0.1, 0.2, and 0.3. **(B)** Stress $\bar{\sigma}_{zz}$ at two ends of the confined cylindrical composite with f = 0.2 for different far-field strains ε_0 = 0, 0.05, 0.1, and 0.2. Symbols are experimental data and solid lines are theoretical prediction (Equations S9 and S10).

2. Temperature-responsive deformation of a curved bilayer structure

We simplify the curved bilayer structure as a planar beam consisting of the passive layer (E_1, h_1, α_1) and the active layer (E_2, h_2, α_2). The curved bilayer structure of width w has an initial radius R_0 and open angle $2\theta_0$, and the passive layer is inside the curved bilayer structure (Supplementary Figure S3A). Since thermal expansion ($\varepsilon_1 = \int_{T_0}^{T} \alpha_1 dT, \varepsilon_2 = \int_{T_0}^{T} \alpha_2 dT$) is uniformly distributed in each layer, the curved structure maintains the arc shape after deformation with its radius changing from R_0 to R_f and open angle changing from $2\theta_0$ to $2\theta_f$. In the following theoretical analysis, subscripts '1' and '2' denote the passive layer and the active layer, respectively.

In the Euler-Bernoulli beam theory, the bilayer structure deforms under the assumption that plane sections remain plane and normal to the axis of the beam. Therefore, the strain ε_y at a distance y from the centroid axis of passive layer is[8]

$$\varepsilon_y = \varepsilon_c + y\Delta\rho, \tag{S11}$$

where ε_c is the unknown strain at the centroid axis of passive layer, $\Delta\rho$ is the change of the curvature of the curved structure upon heating. Under the linear elastic constitutive relations, the stresses σ_1 and σ_2 in these two layers are given by

$$\sigma_1 = E_1(\varepsilon_y - \varepsilon_1), \sigma_2 = E_2(\varepsilon_y - \varepsilon_2), \tag{S12}$$

with E_1 and E_2 the Young's moduli of the passive layer and the active layer, respectively. Since there are no tensions and moments at the beam ends, we have

$$\begin{aligned} \int \sigma \mathrm{d}A &= w\int_{R_0-h_1}^{h_1/2} \sigma_1 \,\mathrm{d}y + w\int_{h_1/2}^{h_2+h_1/2} \sigma_2 \,\mathrm{d}y = 0 \\ \int y\sigma \mathrm{d}A &= w\int_{-h_1/2}^{h_1/2} y\sigma_1 \,\mathrm{d}y + w\int_{h_1/2}^{h_2+h_1/2} y\sigma_2 \,\mathrm{d}y = 0 \end{aligned}, \tag{S13}$$

Substituting Equation S11 into Equation S12, the unknown strain ε_c at the centroid axis of passive layer is solved as

$$\varepsilon_c = \frac{nm^3\varepsilon_2 + nm(nm^3+3m^2+4+6m)\varepsilon_1}{1+n^2m^4+2nm(2+2m^2+3m)}, \tag{S14a}$$

and the change of the curvature is

$$\Delta\rho = \frac{6}{h_1}\frac{nm^2(1+m)(\varepsilon_2-\varepsilon_1)}{1+n^2m^4+2nm(2+2m^2+3m)}, \tag{S14b}$$

with $m = h_1/h_2$, $n = E_1/E_2$. Thus, the radius of curvature of the curved bilayer structure after deformation is[8]

$$R_f = \frac{1+\varepsilon_c}{1+R_0\Delta\rho}R_0, \tag{S15a}$$

and the open angle after deformation is

$$2\theta_f = 2\pi - (1 + R_0\Delta\rho)(2\pi - 2\theta_0). \tag{S15b}$$

The results obtained from Equation S15 are plotted as thick lines in Supplementary Figure S3B and C, agreeing well with our experimental data and finite element simulations in COMSOL Multiphysics®.

It is known that the beam theory is a simplification of the linear elasticity and is more appropriately applicable for thin and long structures. In our case, the bilayer

structure is somewhat thick and its total thickness has the same order of magnitude of its curvature radius. Therefore, it is advisable to check the validity of the above beam modeling using the linear elasticity theory without hypothesizing that the cross sections remain plane and perpendicular to the deflection. In the following theoretical analysis, the bending under the condition of plane strain is analyzed in a polar coordinate (r, θ) (Supplementary Figure S3A), and the Airy stress function related to the stress components is introduced whose expression is chosen so that the equilibrium equations are satisfied automatically. Upon heating, the circular bilayer structure is subjected to pure bending maintaining its arc shape, and consequently the Airy stress function U_k is only related to r-coordinate. Introducing the Airy stress function satisfing $\nabla^4 U_k=0$ (k =1, 2) as follows,

$$U_k = A_k + B_k \ln r + C_k r^2 + D_k r^2 \ln r, \tag{S16}$$

the stress components satisfying the equilibrium equations are given as[9]

$$\begin{aligned} \sigma_{rr}^k &= \frac{1}{r}\frac{\partial U_k}{\partial r} = \frac{B_k}{r^2} + 2C_k + D_k(2\ln r + 1), \\ \sigma_{\theta\theta}^k &= \frac{\partial^2 U_k}{\partial r^2} = -\frac{B_k}{r^2} + 2C_k + D_k(2\ln r + 3), \\ \sigma_{r\theta}^k &= 0, \end{aligned} \tag{S17a}$$

and the corresponding strain components in the polar coordinate are

$$\begin{aligned} \varepsilon_{rr}^k &= \frac{\partial u_r^k}{\partial r} = \frac{1}{E_k}\left[(1+\nu_k)\sigma_{rr}^k - \nu_k\left(\sigma_{rr}^k + \sigma_{\theta\theta}^k\right)\right] + \varepsilon_k, \\ &= \frac{1}{E_k}\left[\frac{1+\nu_k}{r^2}B_k + 2(1-\nu_k)C_k + 2D_k(1-\nu_k)\ln r + D_k(1-3\nu_k)\right] + \varepsilon_k, \\ \varepsilon_{\theta\theta}^k &= \frac{u_r^k}{r} + \frac{1}{r}\frac{\partial u_\theta^k}{\partial \theta} = \frac{1}{E_k}\left[(1+\nu_k)\sigma_{\theta\theta}^k - \nu_k\left(\sigma_{rr}^k + \sigma_{\theta\theta}^k\right)\right] + \varepsilon_k \\ &= \frac{1}{E_k}\left[-\frac{1+\nu_k}{r^2}B_k + 2(1-\nu_k)C_k + 2D_k(1-v)\ln r + D_k(3-\nu_k)\right] + \varepsilon_k, \\ \varepsilon_{r\theta}^k &= \varepsilon_{\theta r}^k = \frac{1}{2}\left(\frac{1}{r}\frac{\partial u_r^k}{\partial \theta} + \frac{\partial u_\theta^k}{\partial r} - \frac{u_\theta^k}{r}\right) = \frac{(1+\nu_k)\sigma_{r\theta}^k}{E_k} = 0, \end{aligned} \tag{S17b}$$

where ν_k = ($3\kappa_k$-$2\mu_k$)/[$2(3\kappa_k$+μ_k)] (k = 1, 2) denotes the Poisson ratio, α_1 = 0.00028 K^{-1} is CTE of silicone, α_2(= α_e in Equation S8) is the effective CTE of the ethanol-silicone composite layer. The displacement components u_r^k and u_θ^k without rigid body motion can be expressed as [9]

$$\begin{aligned} u_r^k &= \frac{1}{E_k}\left\{-\frac{(1+\nu_k)B_k}{r} + 2(1-\nu_k)C_k r + D_k r[2(1-\nu_k)\ln r - (1+\nu_k)]\right\} + r\varepsilon_k, \\ u_\theta^k &= \frac{4D_k}{E_k} r(\theta - \pi), \end{aligned} \tag{S18}$$

with $u_\theta^k = 0$ at $\theta = \pi$ (k = 1, 2).

Since there are zero tension at the inner and outer surfaces, we have $\sigma_{rr}^k = \sigma_{r\theta}^k = 0$ (k = 1, 2) at $r = R_0 - h_1$ and $R_0 + h_2$. Zero total tension and moment at two ends ($\theta = \theta_0$ and $2\pi - \theta_0$) leads to

$$\int_{R_0-h_1}^{R_0+h_2} \sigma_{\theta\theta}^k \, \mathrm{d}r = 0, \ \int_{R_0-h_1}^{R_0+h_2} (r\sigma_{\theta\theta}^k) \, \mathrm{d}r = 0, \ \int_{R_0-h_1}^{R_0+h_2} \sigma_{r\theta}^k \, \mathrm{d}r = 0, \quad (k = 1, 2).$$

(S19a)

The continuities of the tension and displacements at the interface $r = R_0$ require

$$\sigma_{rr}^1 = \sigma_{rr}^2,\ u_r^1 = u_r^2,\ \ u_\theta^1 = u_\theta^2. \tag{S19b}$$

Substituting Equation S17 and S18 into Equation S19, constants B_k, C_k and D_k, can be determined as

$$\begin{aligned}
&D_1 = \frac{E_1 R_0^2}{\eta_3}(\varepsilon_2 - \varepsilon_1), D_2 = \frac{E_2 R_0^2}{\eta_3}(\varepsilon_2 - \varepsilon_1),\\
&C_1 = -\frac{\eta_1 + E_1[2\ln(R_0 - h_1) + 1]}{2\eta_3} R_0^2(\varepsilon_2 - \varepsilon_1),\ C_2 = -\frac{\eta_2 + E_2[2\ln(R_0 + h_2) + 1]}{2\eta_3} R_0^2(\varepsilon_2 - \varepsilon_1),\\
&B_1 = \frac{\eta_1}{\eta_3} R_0^4 (1 - \bar{h}_1)^2(\varepsilon_2 - \varepsilon_1),\ B_2 = \frac{\eta_2}{\eta_3} R_0^4 (1 + \bar{h}_2)^2(\varepsilon_2 - \varepsilon_1),
\end{aligned} \tag{S20a}$$

with

$$\begin{aligned}
\eta_1 =& -\frac{E_1}{2}\frac{[1-(1-\bar{h}_1)^2][(1+\bar{h}_2)^2-1]+4(1+\bar{h}_2)^2\ln(1-\bar{h}_1)\ln(1+\bar{h}_2)}{[(1+\bar{h}_2)^2-1](1-\bar{h}_1)^2\ln(1-\bar{h}_1)+[1-(1-\bar{h}_1)^2](1+\bar{h}_2)^2\ln(1+\bar{h}_2)}\\
&+\frac{E_2}{2}\frac{-[(1+\bar{h}_2)^2-1]^2+4(1+\bar{h}_2)^2[\ln(1+\bar{h}_2)]^2}{[(1+\bar{h}_2)^2-1](1-\bar{h}_1)^2\ln(1-\bar{h}_1)+[1-(1-\bar{h}_1)^2](1+\bar{h}_2)^2\ln(1+\bar{h}_2)},\\
\eta_2 =& \frac{E_1}{2}\frac{[1-(1-\bar{h}_1)^2]^2-4(1-\bar{h}_1)^2[\ln(1-\bar{h}_1)]^2}{[(1+\bar{h}_2)^2-1](1-\bar{h}_1)^2\ln(1-\bar{h}_1)+[1-(1-\bar{h}_1)^2](1+\bar{h}_2)^2\ln(1+\bar{h}_2)}\\
&+\frac{E_2}{2}\frac{[(1+\bar{h}_2)^2-1][1-(1-\bar{h}_1)^2]+4(1-\bar{h}_1)^2\ln(1+\bar{h}_2)\ln(1-\bar{h}_1)}{[(1+\bar{h}_2)^2-1](1-\bar{h}_1)^2\ln(1-\bar{h}_1)+[1-(1-\bar{h}_1)^2](1+\bar{h}_2)^2\ln(1+\bar{h}_2)},\\
\eta_3 =& \frac{R_0^2}{E_2}\{\eta_2[(1+\nu_2)(1+\bar{h}_2)^2 + (1-\nu_2)] + 2E_2[(1-\nu_2)\ln(1+\bar{h}_2) + 1]\}\\
&-\frac{R_0^2}{E_1}\{\eta_1[(1+\upsilon_1)(1-\bar{h}_1)^2 + (1-\upsilon_1)] + 2E_1[(1-\nu_1)\ln(1-\bar{h}_1) + 1]\}.
\end{aligned} \tag{S20b}$$

with $h_1/R_0 = \bar{h}_1, h_2/R_0 = \bar{h}_2$.

The angle $2\theta_f$ of the curved bilayer structure is

$$2\theta_f = 2\theta_0 - \left[\frac{u_\theta^k(r, 2\pi - \theta_0)}{r} - \frac{u_\theta^k(r, \theta_0)}{r}\right] = 2\theta_0 - 8\frac{R_0^2}{\eta_3}(\varepsilon_2 - \varepsilon_1)(\pi - \theta_0). \tag{S21a}$$

By solving $\sigma_{\theta\theta}^1 = 0$, the position of neutral surface in the term of R_n in the passive layer is numerically calculated, which is close to its centroid axis R_0–$h_1/2$. The strain at neutral surface $\varepsilon_{\theta\theta}^1(R_n)$ is then given by Equation S17b. According to $R_0(2\pi - 2\theta_0)[1 + \varepsilon_{\theta\theta}^1(R_n)] = R_f(2\pi - 2\theta_f)$, the curvature radius of the deformed structure is

$$R_f = R_0\frac{\pi - \theta_0}{\pi - \theta_f}\left[1 + \varepsilon_{\theta\theta}^1(R_n)\right]. \tag{S21b}$$

θ_f/θ_0 given by Equation S21a and R_f/R_0 by Equation S21b are plotted in Supplementary Figure S3 as thin lines. Comparing Equation S21a with Equation S15b, the change of the curvature $\Delta\rho$ in Equation S15b is determined as

$$\Delta\rho = 4\frac{R_0}{\eta_3}(\varepsilon_2 - \varepsilon_1), \tag{S22}$$

with the thermal expansion as $\varepsilon_1 = \int_{T_0}^{T} \alpha_1 \mathrm{d}T$ and $\varepsilon_2 = \int_{T_0}^{T} \alpha_2 \mathrm{d}T$.

By ignoring the high-order terms of h_1/R_0 and h_2/R_0, Equation S22 reduces to Equation S14b. In the case of the curvature radius of the curved structure is significantly larger than its thickness, Equation S15 is preferred for its conciseness, and Equation S21 is preferred for its accuracy as the curvature radius is comparable to the structure thickness.

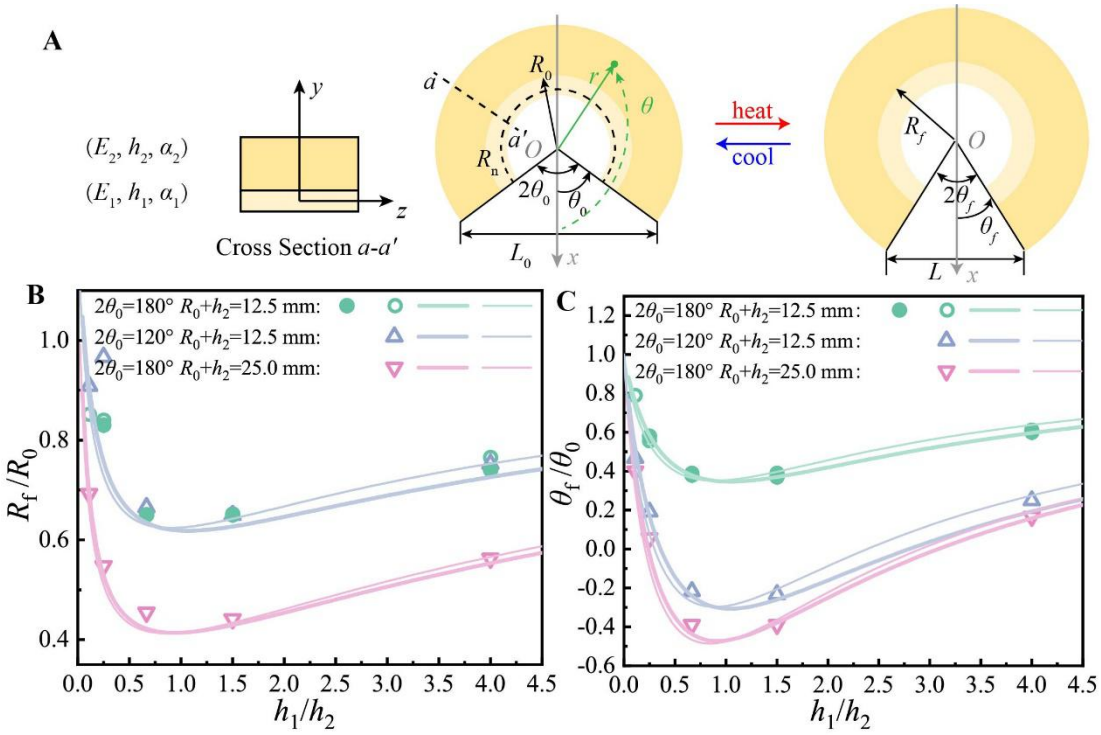

FIG. S3. Temperature-responsive deformation of a circular curved bilayer structure. **(A)** Illustration of the circular curved bilayer structure. Upon heating, the curved structure deforms into another circular arch with the initial interface radius R_0 to R_f and the initial open angle $2\theta_0$ to $2\theta_f$. **(B, C)** Evolution of the radius ratio R_f/R_0 and open angle ratio θ_f/θ_0 as an increasing thickness ratio h_1/h_2 at ΔT = 65 K. Solid symbols are experimental data, open symbols denote simulation results, thick solid lines are theoretical prediction from Equation S15 and thin solid lines are prediction from Equation S21.

3. Materials fabrication and testing

Materials fabrications

In the experiments, Ecoflex 00-35 (Smooth-On, Inc.) is used as the silicon elastomer matrix. Ecoflex 00-30 (Smooth-On, Inc.) and PDMS (SYLGRAD 184, Dow Corning) are used as the passive layer. The precursors of Ecoflex 00-35 or Ecoflex 00-30 are mixed under the volume fraction of 1:1 and cured at room temperature, with Ecoflex 00-35 curing for 5 minutes, and Ecoflex 00-30 curing for 4 hours. For PDMS, the Sylgrad-184A is mixed with Sylgrad-184B under the mass fraction of 10:1, and then the mixture is curing at 60 ℃ for 12 hours. As show in Supplementary Figure S4, the fabrication of the soft actuators roughly includes the following three steps. The precursors (volume fraction of 1:1) of Ecoflex 00-35 are

mixed with the ethanol for 4 minutes at first (Step 1). Then, the mixture is poured into a mold with resistance wire embedded and cured at room temperature for 5 minutes (Step 2). Finally, the soft actuators are removed from the mold and powered electrically to achieve locomotion (Step 3). In Step 2, the passive layer made of Ecoflex 00-30 or PDMS is pre-cured and placed inside the mold, then the uncured mixture of ethanol and silicon rubber (Ecoflex 00-35) is poured into the mold and cured together with the passive layer.

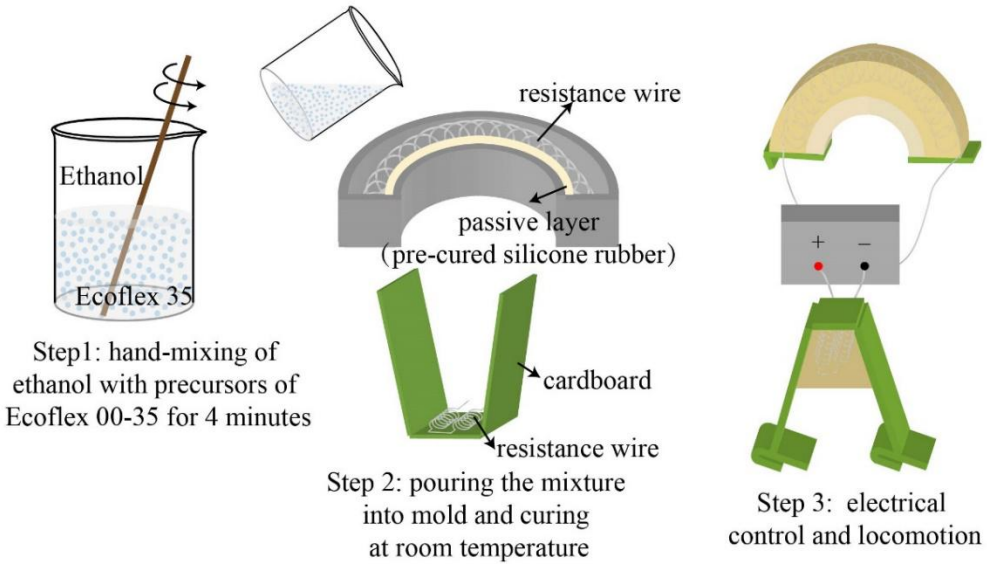

FIG. S4. Fabrication process of soft robots.

Uniaxial tension/compression

A sample with a sectional dimension of 5 mm × 5 mm is inserted into a heating tube (inner diameter of 10 mm) without touching with the side wall of the tube. After the sample is fixed on the fixture, turn on the heating tube until the temperature reaches the specific temperature. Waiting for another 5 minutes until the temperature is constant, and then carry out the uniaxial tension/compression experiment.

Thermal expansion testing in a rigid container

A cylindrical composite sample of diameter 6 mm is inserted into a rigid heating tube of an inner diameter 6 mm and length 20 mm with two force gauges attached at two ends. The confined sample of a shorter length than the confining tube can only expand in the axial direction due to the circumferential constraint. Upon heating, the sample first expands freely in the axial direction and then contacts with the force gauges at a sufficiently high temperature. At a prescribed temperature, the contact force is measured as the sample stops its expansion.

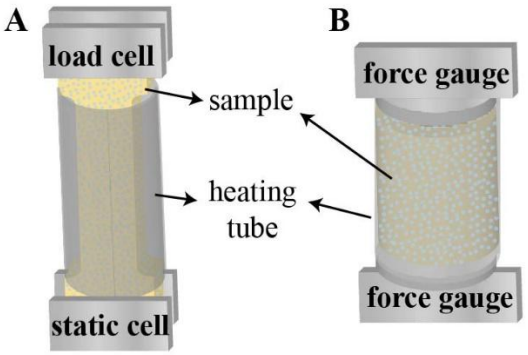

FIG. S5. Illustration of experimental setups. Uniaxial tension/compression testing **(A)** and thermal expansion testing **(B)** of the ethanol-silicone composites. The mechanical testing is conducted with MTI Instruments (MTESTQuattro, ADMET Inc.).

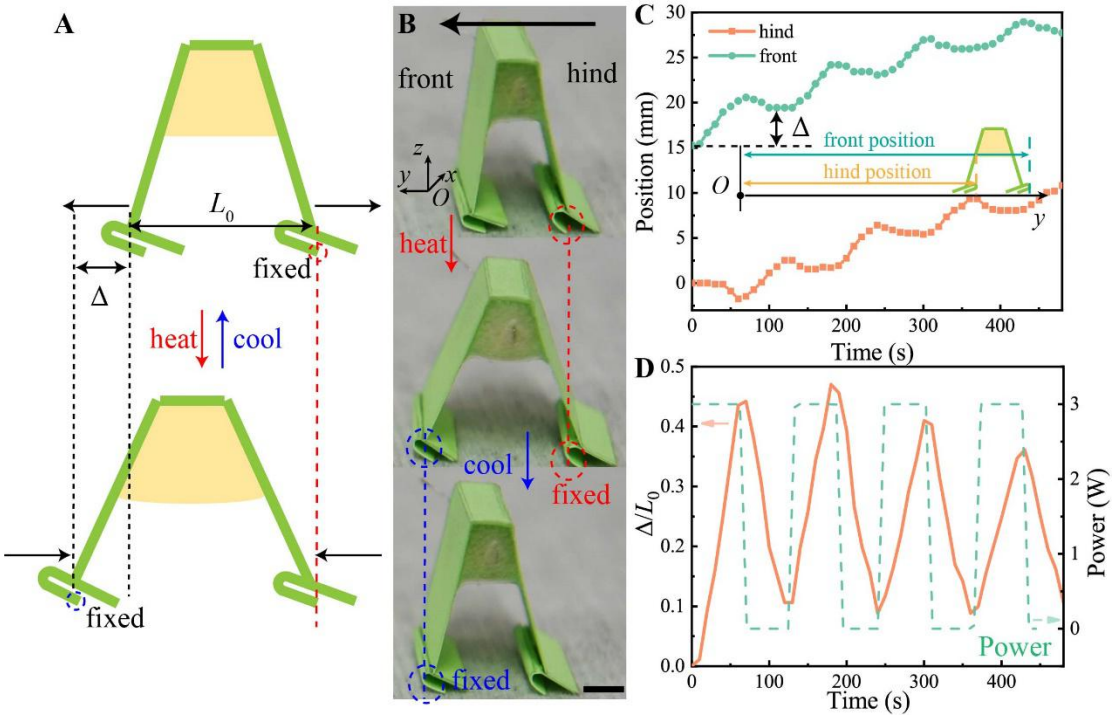

FIG. S6. Crawling of self-folding structures with attached tips. **(A)** Locomotion illustration. **(B)** Crawling of the self-folding structure in one heating-cooling cycle. Similar to the inchworm robot, the asymmetrical friction between the attached sheets and substrate allows unidirectional locomotion. Upon heating the hind leg of the structure is fixed and foreleg slides forward; upon cooling the foreleg is fixed and the hind leg slides forward. Scale bar: 5 mm. **(C)** Position evolution of the sheets attached on the foreleg and hind leg (shown as the inset). **(D)** Temporal evolution of the relative displacement Δ/L_0. In one cycle, the self-folding structure with side angle $\xi = 85°$ achieves a relative displacement Δ/L_0 around 0.45 (solid line), and the corresponding locomotion speed is about 0.10 mm/s. The dashed line is the temporal variation of the input power from the resistance wire embedded in the soft joint.

Table S1. Geometry and displacement information of walking robots and caterpillars.

Control methods	ε	h (mm)	L_0/h	Δ/L_0	References
Light	0.0045	0.37	27.027	0.022	[10]
	0.019			0.096	
	0.0252			0.112	
	0.031			0.117	
	0.003	0.001	30000	0.196	[11]
	0.625	0.01	800	0.337	[12]
				0.1	
	0.2	0.25	40	1	[13]
	0.55	0.3	60	0.91	[14]
	0.5	0.002	60	1	[15]
	0.78	0.13	76.923	0.330	[16]
Pneumatic	0.3	20	5	0.190	[17]
DEAs	0.01	0.5	286	0.041	[18]
Heat	1E-4	2E-6	1000	1	[19]
	0.3	2	32	0.025	[20]
	0.7	3.2	20	0.363	[21]
	0.24	0.5	57.2	0.070	[22]
	0.03	0.6	100	0.220	[23]
	0.02			0.130	
	0.01			0.015	
	0.2	0.05	290	0.055	[24]
	0.02	0.75	13.333	0.466	[25]
	0.4	0.4	100	1	[26]
Magnetic	0	0.1	80	3.5E-4	[27]
Electric	0.6	0.4	62.5	0.400	[28]
	0.01	0.35	51.428	0.227	[29]
	0.018	0.45	34.888	0.380	[30]
Humidity	0.04	0.06	416.666	0.342	[31]
Base oscillations	0.005	2	10	0.005	[32]
	0.01			0.010	
	0.015			0.015	
	0.02			0.020	
	0.025			0.025	
Vacuum	0.493	0.25	400	0.493	[33]
	0.68			0.680	
Light rectilinear motion	0.2	0.05	6	0.044	[34]
	0.048	0.2	5	0.044	[35]
	0.16	0.07	385.714	0.048	[36]
Caterpillars	0.258	1.87	9.090	0.258	[37]
	0.25	3.45	6.956	0.250	
	0.161	5	5.20	0.162	

References

[1] Dillon HE, Penoncello SG. A fundamental equation for calculation of the thermodynamic properties of ethanol. Int J Thermophys 2004;25:321-335.

[2] Overvelde JTB, Dykstra DMJ, de Rooij R, *et al*. Tensile instability in a thick elastic body. Phys Rev Lett 2016;117:094301.

[3] Lee TI, Kim MS, Kim TS. Contact-free thermal expansion measurement of very soft elastomers using digital image correlation. Polym Test 2016;51:181-189.

[4] Duan HL, Wang J, Huang ZP, *et al*. Eshelby formalism for nano-inhomogeneities. Proc Royal Soc A 2005;461:3335-3353.

[5] Duan HL, Wang J, Huang ZP, *et al*. Size-dependent effective elastic constants of solids containing nano-inhomogeneities with interface stress. J Mech Phys Solids 2005;53:1574-1596.

[6] Duan HL, Karihaloo BL. Thermo-elastic properties of heterogeneous materials with imperfect interfaces: generalized Levin's formula and Hill's connections. J Mech Phys Solids 2007;55:1036-1052.

[7] Levin VM. Thermal expansion coefficients of heterogeneous materials. Mech Solids 1967;2:58-61.

[8] Zhang H, Guo X, Wu J, *et al.* Soft mechanical metamaterials with unusual swelling behavior and tunable stress-strain curves. Sci Adv 2018;4:eaar8535.

[9] Timoshenko SP, Goodier JC, Theory of Elasticity. New York: McGraw-Hill, third edition, 1970.

[10] Kizilkan E, Strueben J, Staubitz A, *et al.* Bioinspired photocontrollable microstructured transport device. Sci Robot 2017;2:eaak9454.

[11] Kwan KW, Li SJ, Hau NY, *et al*. Light-stimulated actuators based on nickel hydroxide-oxyhydroxide. Sci Robot 2018;3:eaat4051.

[12] Zeng H, Wani OM, Wasylczyk P, *et al.* Light-driven, caterpillar-inspired miniature inching robot. Macromol Rapid Commun 2018;39:700224.

[13] McBride MK, Martinez AM, Cox L, *et al.* A readily programmable, fully reversible shape-switching material. Sci Adv 2018;4:eaat4634.

[14] Liu Y, Shaw B, Dickey MD, *et al.* Sequential self-folding of polymer sheets. Sci Adv 2017;3:e1602417.

[15] Mu J, Hou C, Wang H, *et al.* Origami-inspired active graphene-based paper for programmable instant self-folding walking devices. Sci Adv 2015;1:e1500533.

[16] Wang E, Desai MS, Lee SW. Light-controlled graphene-elastin composite hydrogel actuators. Nano Lett 2013;13:2826-2830.

[17] Terryn S, Brancart J, Lefeber D, *et al.* Self-healing soft pneumatic robots. Sci Robot 2017;2:1-12.

[18] Christianson C, Goldberg NN, Deheyn DD, *et al*. Translucent soft robots driven by frameless fluid electrode dielectric elastomer actuators. Sci Robot

2018;3:eaat1893.
[19] Miskin MZ, Dorsey KJ, Bircan B, *et al*. Graphene-based bimorphs for micron-sized, autonomous origami machines. Proc Natl Acad Sci USA 2018;115:466-470.
[20] Wisinger CE, Maynard LA, Barone JR. Bending, curling, and twisting in polymeric bilayers. Soft Matter 2019;15:4541-4547.
[21] Kang DJ, An S, Yarin AL, *et al.* Programmable soft robotics based on nano-textured thermo-responsive actuators. Nanoscale 2019;11:2065-2070.
[22] Wang C, Sim K, Chen J, *et al.* Soft ultrathin electronics innervated adaptive fully soft robots. Adv Mater 2018;30:1706695.
[23] Ding Z, Yuan C, Peng X, *et al.* Direct 4D printing via active composite materials. Sci Adv 2017;3:e1602890.
[24] Rogóż M, Zeng H, Xuan C, *et al.* Light-driven soft robot mimics caterpillar locomotion in natural scale. Adv Opt Mater 2016;4:1689-1694.
[25] Taccola S, Greco F, Sinibaldi E, *et al*. Toward a new generation of electrically controllable hygromorphic soft actuators. Adv Mater 2015;27:1668-1675.
[26] Behl M, Kratz K, Zotzmann J, *et al.* Reversible bidirectional shape-memory polymers. Adv Mater 2013;25:4466-4469.
[27] Li M, Wang Y, Chen A, *et al.* Flexible magnetic composites for light-controlled actuation and interfaces. Proc Natl Acad Sci USA 2018;115:8119-8124.
[28] Osada Y, Gong JP. Soft and wet materials: polymer gels. Adv Mater 1998;10:827-837.
[29] Yan Y, Santaniello T, Bettini LG, *et al.* Electroactive ionic soft actuators with monolithically integrated gold nanocomposite electrodes. Adv Mater 2017;29:1606109.
[30] Must I, Kaasik F, Poldsalu I, *et al.* Ionic and capacitive artificial muscle for biomimetic soft robotics. Adv Eng Mater 2015;17:84-94.
[31] Shin B, Ha J, Lee M, *et al*. Hygrobot: a self-locomotive ratcheted actuator powered by environmental humidity. Sci Robot 2018;3:eaar2629.
[32] Mahadevan L, Daniel S, Chaudhury MK. Biomimetic ratcheting motion of a soft, slender, sessile gel. Proc Natl Acad Sci USA 2004;101:23-26.
[33] Li S, Vogt DM, Rus D, *et al*. Fluid-driven origami-inspired artificial muscles. Proc Natl Acad Sci USA 2017;114:13132-13137.
[34] Zeng H, Wasylczyk P, Parmeggiani C, *et al.* Light-fueled microscopic walkers. Adv Mater 2015;27:3883-3887.
[35] Palagi S, Mark AG, Reigh SY, *et al*. Structured light enables biomimetic swimming and versatile locomotion of photoresponsive soft microrobots. Nat Mater 2016;15:647-653.
[36] Liu X, Kim SK, Wang X. Thermomechanical liquid crystalline elastomer

capillaries with biomimetic peristaltic crawling function. J Mater Chem B 2016;4:7293-7302.
[37] Brackenbury J. Fast locomotion in caterpillars. J Insect Physiol 1999;45:525-533.